Development of New Optical Adjustment System for FITE: Far-infrared Interferometric Telescope Experiment

宇宙遠赤外線干渉計 FITE のための 新しい光学調整システムの開発

Ayana SASAKI

A Dissertation for the Degree of Doctor of Philosophy

Department of Earth and Space Science,
Graduate School of Science, Osaka University
February 2020

Abstract

One of the important problems in astrophysics is how planets form. The easiest way to understand their formation process is to directly observe their forming environment called protoplanetary disks. In order to directly observe the temperature distribution of a protoplanetary disk, it is necessary to observe high-resolution imaging at one arcsec at the thermal emissions (mainly far-infrared) from interstellar dust. However, observation with high-spatial resolution in the far-infrared wavelength band is difficult to achieve because it is necessary to launch a large-diameter telescope in space.

In order to study the formation of planets in protoplanetary disks, we have developed a balloon-borne far-infrared interferometer, FITE (Far-infrared Interferometric Telescope Experiment). The final goal of spatial resolution was one arcsec at 100 μm. As a first step, we aimed to achieve a spatial resolution of five arcsecs at 155 μm with a 6-m baseline. FITE is a two-beam interferometer like the Michelson's stellar interferometer. Positions and attitudes of all mirrors were required to have their alignment checked and possibly adjusted before launch and were checked during observation. We had to satisfy three requirements: the coincidence of the phases of each beam (wavefront error), image quality of the two beams at the (common) focus, and no optical path difference between the two beams for celestial objects. In order to achieve the former two requirements, we developed an interferometer adjustment system that used a newly developed interferometer measurement instrument. This instrument adopted a Shack-Hartmann wavefront sensor to measure wavefront errors of the two off-axis parabolic mirrors, simultaneously. With this system, the adjustment of the FITE interferometer was carried out at the Alice Springs balloon base in Australia as the JAXA's Australia balloon experiment campaign of 2018. On-site adjustment was successful; wavefront errors of the two off-axis parabolic mirrors were 1.78 μm and 4.99 μm (peak-to-valley), and the Hartmann constant was 13 arcsecs. As for the optical path difference, we achieved the requirement by step-wise displacement of a folding plane mirror. There results satisfied the requirements for an interferometer designed for a wavelength of 155 μm. Improvement of spatial resolution at far-infrared wavelengths is undoubtedly important for research on protoplanetary disks, circumstellar dust shells of late-type stars, and star-forming galaxies. The method we have developed is also useful for future space interferometers.

Contents

List of Figures

Chapter 1

1 Introduction

One of the most intriguing problems in astrophysics is how planets form. In the solar system, the most familiar planetary system, there are eight planets around the sun. Of the planets in the solar system, the only one confirmed to have life is Earth. Many telescopes around the world have been observing the skies to answer the question of whether a planet with Earth-like life is in this universe. An extrasolar planet was first discovered in 1995 (Mayor et al., 1995). Numerous exoplanets have been discovered since then, but many of the discovered exoplanets are dissimilar to any of the solar system planets. For instance, the first exoplanet discovered has about half the mass of Jupiter and orbits its central star in just four days (Mayor et al., 1995). These discovered planets plagued many researchers because they could not be explained by standard planetary theory (Hayashi et al., 1985). The simplest way to understand the planet formation mechanism is to directly observe the protoplanetary disk: the site where the planets are formed. However, because current observation techniques are not enough to research the protoplanetary disk at far-infrared wavelength bands, improvements in the observation techniques are essential (See Sec. 1.1).

In this section, the basics of protoplanetary disks are explained, and items required for telescopes for an observing of high spatial resolution in the far-infrared wavelength band are described.

1.1 Protoplanetary disks

The protoplanetary disk is a site of the planet formation and be said to be the initial condition for producing various planetary systems. A protoplanetary disk is mainly made of hydrogen molecular gas, just like molecular clouds. In addition to gas, the disk contains dust (Wyatt, 2008). Dust are considered to be materials originating from rocky planets such as the Earth. The surface density distribution (mass) and temperature distribution of the disk have an important effect on the planet formation process. Fig. 1.1 shows a schematic view of the star and disk formation process. The four different stages, class 0 – III stellar sources, are identified from the observed infrared excess relative to a

blackbody spectrum (Nicolas D., et al., 2011). At the youngest protostellar stage ($t < 0.03$ My), called Class 0, the central object is surrounded by a dense envelope. As accretion proceeds, the envelope becomes tenuous and forms a disk. This late accretion phase is called the Class I ($t \sim 0.2$ My) stage. When the envelope is exhausted, the disk becomes optically visible. This is the Class II ($t \sim 1$ My) stage. Eventually, this protoplanetary disk disappears and becomes a diskless star called the Class III stage ($t \sim 10$ My).

In recent years, the theory of the planet formation in the solar system has succeeded in explaining the formation process of giant gas planets such as Jupiter, rocky planets, and ice planets by using numerical simulations. In addition, this theory has succeeded in predicting the birth of various planetary systems by changing the surface density distribution, heavy element content, central star mass and luminosity (Ida et al., 2005).

Observations of protoplanetary disks have also made significant progress through observations in the infrared and submillimeter wavelength bands. In direct observations of dust in the protoplanetary disks, the main observation wavelengths are near-infrared and submillimeter wavelength bands that can be observed from the ground. For instance, scattered light from dust of 1 μm size is observed in protoplanetary disks at a near-infrared observation with the Subaru Telescope (Fukagawa et al., 2006). Also, ground-based the Atacama Large Millimeter Array (ALMA) has discovered the presence of 1 mm dust in protoplanetary disks at submillimeter waves (ALMA Partnership, 2015). Recent studies have revealed the diversity of infrared emission spectra (reflecting the diversity of the disk structure) from disks, suggesting the complexity of the temperature distribution inside the disk (Hillenbrand et al., 2008). These disks differ from standard disks in terms of disk shape, size, temperature distribution, total mass, and heavy element content. To discuss the formation process of Earth-like planets, it is necessary to study initial conditions for disks.

However, the understanding of the properties of the protoplanetary disks based on the observations is far from enough to constrain the theory of planet formation. To understand major properties such as temperature distribution and surface density distribution of the disk, it is important to observe the spatially resolved protoplanetary disk. Near-infrared wavelength bands can detect the scattered light from dust so that the size and shape of the disk can be known directly. Mid-infrared and far-infrared wavelength bands can observe the peak of the thermal radiation from low-temperature dust (30–300 K) to assess the temperature distribution of dust in the disk. Submillimeter and millimeter wavelength

bands can identify the total mass and surface density distribution of the disk (Shibai et al., 2009). Observing at multiple wavelengths reveals various information about the protoplanetary disk. Therefore, the understanding of the planetary formation in the protoplanetary disk has been advanced by multiwavelength observation.

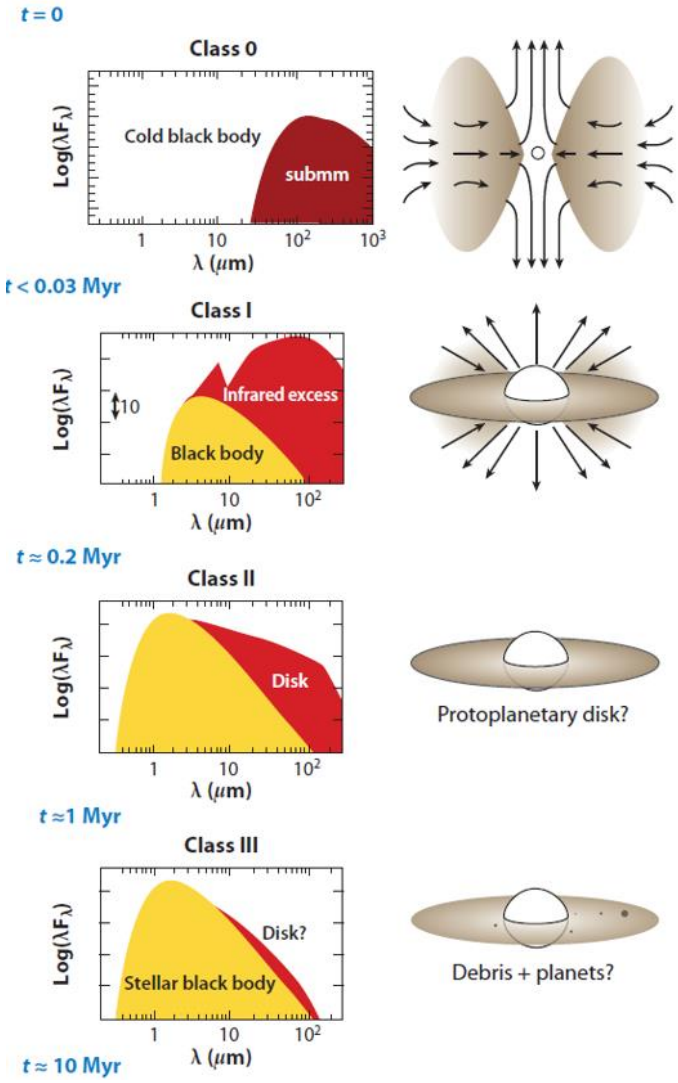

Fig. 1.1 Schematic view of star and disk formation process. The four different stages, class 0 – III stellar sources, are identified from the observed infrared excess relative to a blackbody spectrum (Dauphas et al., 2011).

Of these wavelengths, far-infrared wavelength bands require the technological development. In the absence of detailed imaging at far-infrared wavelength bands, the majority of information about a disk is derived from the star's spectral energy distribution (SED), which includes emission from nearby dust heated by the star (Wyatt, 2008). It is

quite difficult to derive the detailed structure only from the comparison between the far-infrared SED and the disk model, and the lack of resolution leaves uncertainty in the conclusion. As an example, HL Tau has one of the typical protoplanetary disks, which is at a distance of 140 pc from the Earth. The size of its protoplanetary disk is about 200 AU in diameter (ALMA Partnership, 2015). The disk size of 200 AU at 140 pc corresponds to 1.5 arcsec in spatial resolution, meaning that the disk cannot be spatially decomposed without performing observations with a spatial resolution of one arcsec. To understand the planetary formation process in the disk, it is necessary to observe with a spatial resolution of a sub-arcsecond. The resolution at the near-infrared wavelength is already achieved at about 0.1 arcsec (Muto et al., 2012). The resolution of at the submillimeter wavelength has been achieved at has achieved one arcsec with the Submillimeter Array (SMA) (ALMA Partnership, 2015). Since the SMA is an interferometer that performs observations by deploying telescope groups on the ground, the resolution will increase dramatically with future ALMA observations. Since these wavelength bands can be observed from the ground, it is possible to observe with high spatial resolution by increasing the size of the telescope or extending the baseline. However, it is difficult to increase the spatial resolution in the far-infrared wavelength band that cannot be observed from the ground. The observation with the highest spatial resolution in the far-infrared wavelength band was performed by the Herschel Space Telescope launched in 2009 (Pilbratt et al., 2010). Herschel achieves a spatial resolution of 10 arcsec at far-infrared wavelengths (Pilbratt et al., 2010). With this spatial resolution, the protoplanetary disk cannot be disassembled and observed. In other words, since the spatial resolution is insufficient only in the far-infrared wavelength band, the surface density distribution of low-temperature interstellar dust cannot be known from direct observation.

1.2 Importance of high-spatial resolution at far-infrared wavelength

In astronomy, improvements in spatial resolution have been extremely important, not only for gathering details of known celestial objects but also for unexpected discoveries. For example, the ALMA interferometer has observed protoplanetary disks with extremely high spatial resolution. One of the remarkable observational results is that the continuum of images at wavelengths of 2.9, 1.3, and 0.87 mm, having unprecedented angular resolutions of 0.075 arcsec (10 AU) – 0.025 arcsec (3.5 AU), have revealed an astonishing

level of detail in the circumstellar disk surrounding the young solar analog, HL Tau. They have revealed a pattern of bright and dark rings observed at all wavelengths (ALMA Partnership et al., 2015). This observation has brought considerable progress to the study of the formation of planetary systems, suggesting that this gap may be the result of planetary formation in the disk. The high spatial resolution of the ALMA interferometer has made it possible to resolve and observe the gap structure in the disk. In addition, regarding the spread and shape of the disk, a precise observation has been performed at near-infrared wavelengths with the Subaru Telescope, the Keck telescope, and others.

The role of far-infrared observation is also important because thermal radiation from dust, the material of planets, has a peak in the mid-infrared and far-infrared wavelength bands. Protoplanetary disk temperatures vary considerably depending on the disk's surface density distribution and distance from a central star. Therefore, if far-infrared wavelength observations at a high spatial resolution are possible, it is expected that the temperature and surface density distributions can be determined, which reveals the evolutionary process from protoplanetary disk to planetary system. It is expected that high-resolution far-infrared observations will make an important contribution to the detailed research of circumstellar shells of late-type stars and star-forming galaxies.

However, the observation at high spatial resolutions of far-infrared wavelengths is not easy. Because the spatial resolution is limited by the diffraction-limited of the telescope and degrades in proportion to the wavelength. The diffraction limit spatial resolution $\Delta\theta$ obtained by a telescope with a circular aperture is $\Delta\theta = 1.22\ \lambda/D$, where λ is the wavelength and D is the diameter of the telescope. From this equation, increasing the spatial resolution for a specific wavelength requires determining the size of a telescope with diameter D. For example, even with the 3.5-m diameter Herschel Space Telescope (Pilbratt et al., 2010), the 2.5 m-diameter SOFIA telescope (Becklin, 2005), and the planned 2.5-m diameter SPICA (Roelfsema et al., 2018), the resolution at wavelength 100 μm is approximately 10 arcsec in order of magnitude. This contrasts with visible light, near-infrared, and submillimeter wavelength bands, in which the milliarcsecond resolultion is achieved. In the submillimeter and millimeter wavelength bands, in which the wavelengths are longer than those in the far-infrared wavelength band, very high spatial resolution is achieved by using ground-based interferometers. The interferometer can obtain a high spatial resolution by interfering electromagnetic waves combining two or more small-aperture telescopes at a distance (the distance is called the baseline). The

diffraction-limited spatial resolution $\Delta\theta$ is $\Delta\theta = 1.22\ \lambda/B$, where λ is the wavelength and B is the baseline of the telescope.

Even worse, observations at far-infrared wavelengths require taking a telescope into outer space that is not affected by the absorption of radiation by the Earth's atmosphere. Fig. 1.2 shows atmospheric transmission over 1 – 1000 μm. The atmosphere is mostly opaque in the mid-infrared wavelengths through the far-infrared wavelengths. In addition, the figure shows a comparison of atmospheric transmission expected for the ground-based observation with ALMA, the observation with SOFIA, and those at two higher altitudes that are accessible by balloon-based platforms (Farrah et al., 2019). As shown in Fig. 1.2, the absorption of the Earth's atmosphere can be ignored if observations are made possible at the high altitude of the balloon.

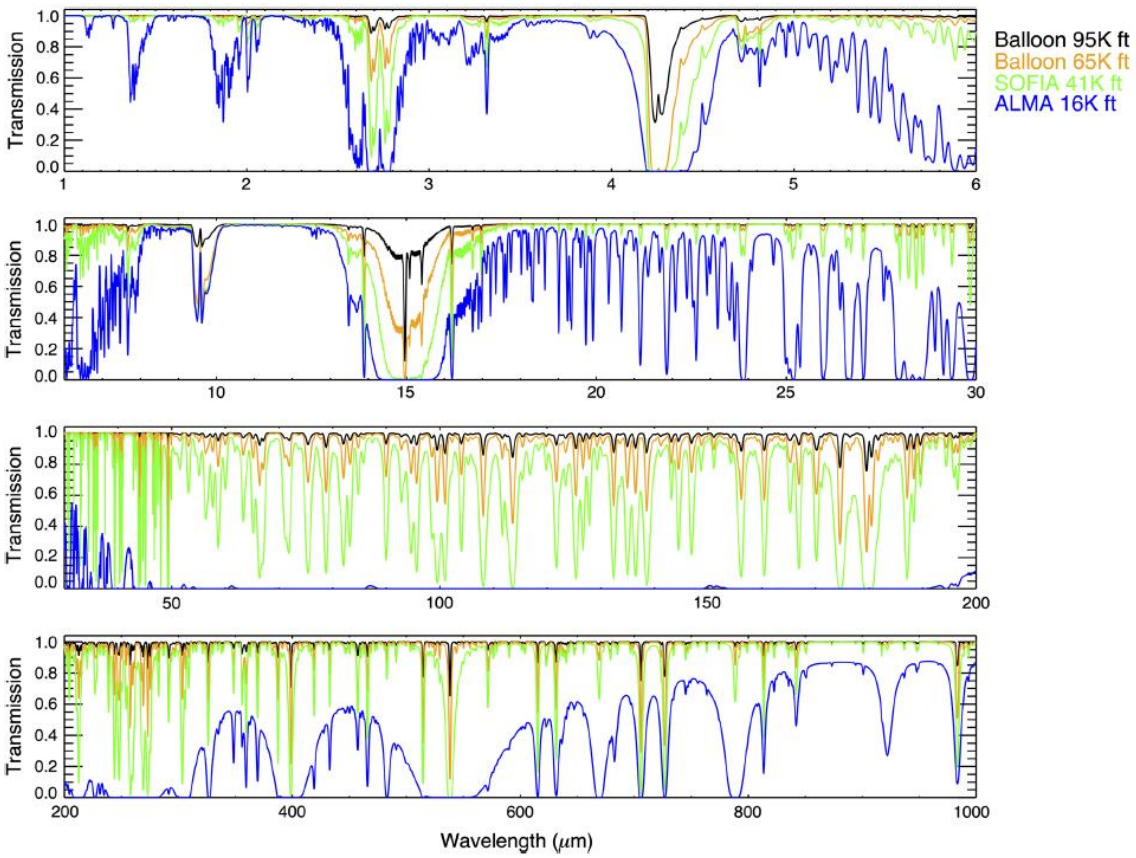

Fig. 1.2 Simulation of atmospheric transmission over 1 to 1000 μm. The precipitable water vapor for ALMA (5060 m), SOFIA (12,500 m), and the 19,800m and 29,000m altitudes are 500, 7.3, 1.1, and 0.2 μm, respectively. The atmosphere is mostly opaque in the mid-infrared wavelengths through the far-infrared wavelengths. (Farrah, D.,

Based on these attitudes described above, in order to perform the observations with a spatial resolution of less than one arcsec at the far-infrared wavelength of 100 μm, it is necessary to launch a telescope with a diameter of 20 m above the balloon altitude. Realizing this large telescope in space is impractical. For this reason, there is no choice but to perform observations with a space interferometer by combining small-diameter mirrors that enables a high-resolution observation. In Europe and the United States, a space interferometer project has been formulated with the aim of launching in the 2040s, and technology development continues. For instance, NASA envisions the Space Infrared Interferometric Telescope, SPIRIT (Leisawitz et al., 2007), as a far-infrared interferometer plan (Farrah et al, 2019). In addition, ESA envisions the other space interferometer projects, FIRI (Helmich et al., 2007), and the Exploratory Submm sPace Radio-Interferometric Telescope, ESPRIT (Wild et al., 2008). However, since space interferometers need floating and remote observations, there are many technical steps to make them successful. To achieve high spatial resolution at the far-infrared wavelength, the Balloon Experimental Twin Telescope for Infrared Interferometry (BETTII)—an 8 m-baseline, balloon-borne interferometer—was developed and launched in 2017 for an engineering flight (Rinehart et al., 2018). Unfortunately, the flight ended with an anomaly that resulted in destruction of the payload (Rinehart et al., 2018).

1.3 Our approach: FITE Project

To achieve high spatial resolution at far-infrared wavelength, we have developed a balloon-borne far-infrared interferometer, FITE (Shibai et al., 2010). Since the earth's atmosphere is completely opaque in these wavelength bands, it is necessary to launch the telescope into space or the stratosphere. FITE will be launched into the stratosphere with a scientific balloon to perform the far-infrared observation. The first flight was scheduled as an experiment of the JAXA's Australia balloon experiment campaign in 2018. Unfortunately, due to bad weather and the delay in the preparation, FITE did not flight in 2018. The left panel of Fig. 1.3 shows the hanging test of FITE, which was conducted before launch. This test, in which FITE was suspended by a hoist crane on the launching vehicle, simulates the state when FITE is hang by a balloon at high altitudes. The right panel of Fig. 1.3 shows the light paths during the observation. The two light beams from

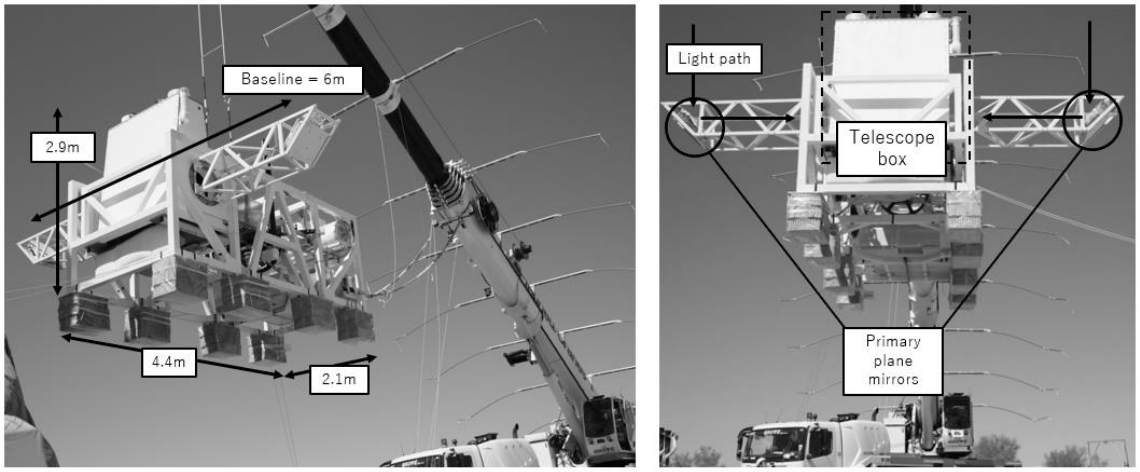

Fig. 1.3 (L) Hanging test of FITE. (R) Light beams from a celestial object are reflected by the two primary plane mirrors mounted on each end of the baseline and enter on secondary plane mirrors, then, reflect off two off-axis parabolic mirrors in the telescope box. The detailed diagram of the light paths is shown in Fig. 1.3.

a celestial object are reflected by the two primary plane mirrors placed on each end of the baseline, are incident on the two secondary plane mirrors, and then, reflect off the two off-axis parabolic mirrors in the telescope box.

The goal of FITE is to achieve one arcsec spatial resolution at 100 μm. In order to achieve this resolution, the baseline will be extended to 20-m (Shibai et al., 2010). For the first flight planned in 2018, FITE baseline was 6-m at 155 μm. At this baseline, the FITE spatial resolution corresponded to five arcsecs. The reason for choosing 155 μm wavelength was that we had a sensitive far-infrared sensor and an appropriate bandpass filter for the sensor, and that the wavelength of 155 μm makes sense for the future goal of far-infrared interferometer in space.

The basic design of FITE is similar to the Michelson's stellar interferometer (Michelson and Peace, 1921). The stellar diameter can be measured by acquiring a visibility curve, a curve of the change in the sharpness of the interference fringe with respect to the baseline (Quirrenbach et al., 1996). The fringe contrast is historically called the visibility. The visibility depends on the spatial frequency, that is, the baseline (Monnier 2003). Hence, the fine structure of celestial object can be measured by changing the baseline and observing the visibility. See Matsuo et al. (2008) for the method of measuring the stellar diameter by FITE.

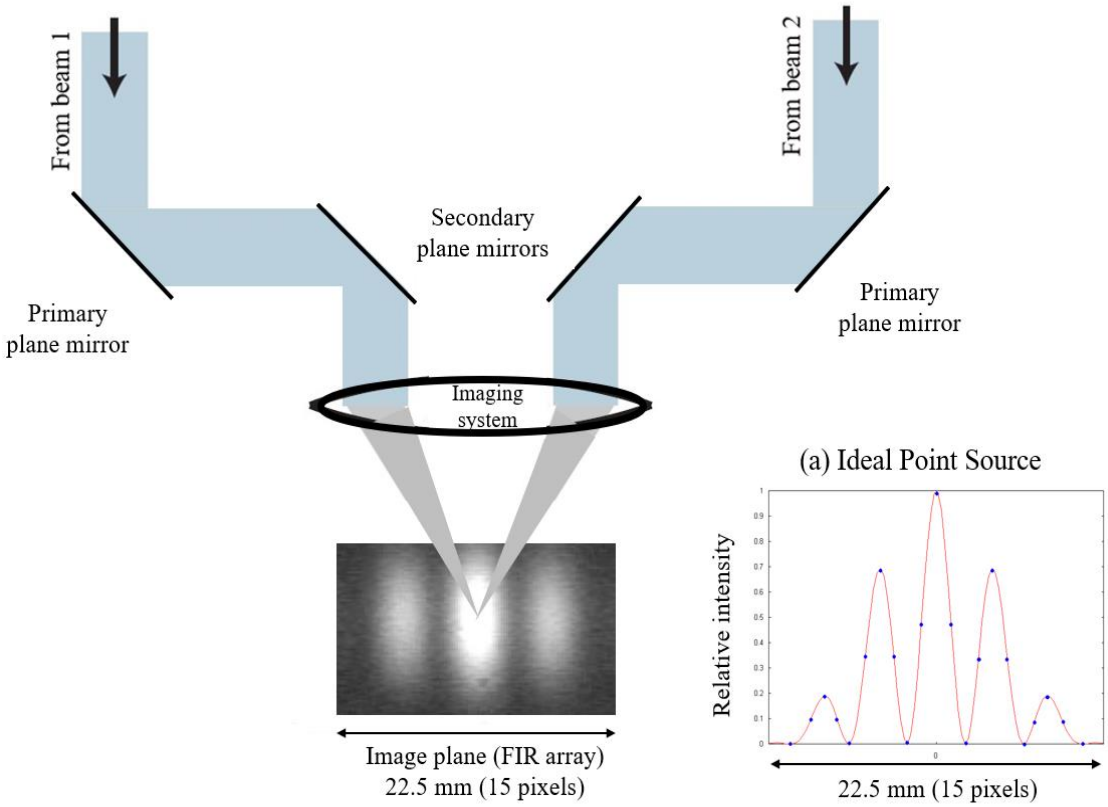

Fig. 1.4 A conceptual diagram of the FITE interferometer optics and the ideal interference fringe pattern on the image plane. (a) The results of simulating the fringe patterns appear on the image plane when observing an ideal point source (Kato et al., 2009).

Fig. 1.4 shows a conceptual diagram of the FITE interferometer optics, and diagram of all FITE optics is shown in Fig. 1.5. The FITE interferometer optics is composed of four plane mirrors and two off-axis parabolic mirrors. The results of simulating the fringes appear on the image plane when observing an ideal point source is shown in Fig. 1.4(a).

In order to detect the interference fringes at far-infrared wavelengths, an interferometer adjustment for FITE was necessary (see Section 2), both before launch and during observation. The purpose of developing the interferometer adjustment method for FITE was to complete the adjustment before launch in a short time, which was conventionally carried out over several weeks (Sasaki et al., 2012). Finally, Sasaki et al. (2014) devised the method and developed the mirror adjustment instrument with a Shack-Hartmann wavefront sensor. The Shack-Hartmann wavefront sensor is not often used in the adjustment of installed

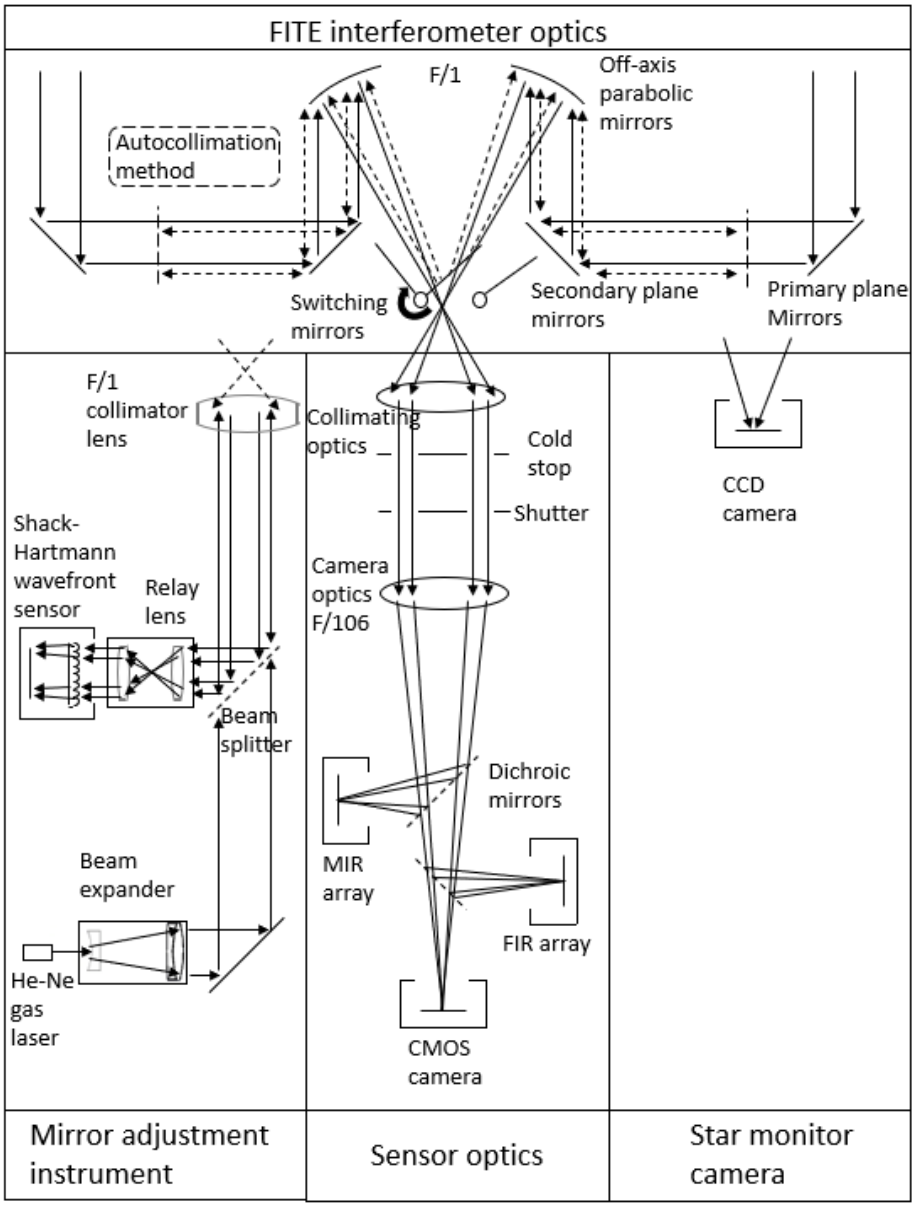

Fig. 1.5 Diagram of all the FITE optical system. The FITE optical system has four optics: the FITE interferometer optics used for collecting light from a celestial object, the mirror adjustment instrument used for adjustment (see Sec. 2), the sensor optics used for astronomical observation (Kohyama et al., 2009), and the star monitor camera used for attitude control of the FITE gondola. These optical systems are part of the in-flight equipment. However, the mirror adjustment instrument is only used before launch and not used during flight. Each optical system shown in bottom is switched by inserting and removing two switching mirrors placed in front of the first focal point. The light is vent by 90 degrees by switching mirror. Thus, the actual configuration of the mirror adjustment instrument and the star monitor camera is rotated by 90 degrees. Each optical system shown bottom is switched by inserting and removing two

optics, but it is widely used as a sensor in adaptive optics. For example, the laser guide star adaptive optics module of the Subaru telescope has a Shack-Hartmann wavefront sensor (Watanabe et al., 2004), as does the W. M. Keck observatory laser guide star adaptive optics system (Wizinowich et al., 2006).

This thesis describes the newly devised FITE interferometer adjustment method (Sec 2.1), newly FITE interferometer adjustment instrument (Sec 2.2) designed based on the method, and the adjustment results of using FITE interferometer adjustment system (Sec. 2.3).

2 New optical adjustment system for FITE

Section 2.1 describes the SPIE paper (Sasaki et al., 2012), Section 2.2 describes the IEEE paper (Sasaki et al., 2014), and Section 2.3 describes the Journal of Astronomical Instrumentations paper content (Sasaki et al., 2019). The latest information of the new optical adjustment system for FITE is given in Section 2.3. The major differences between the three papers are the required accuracy described in the thesis in section 2.1 and Section 2.2, and some of the elements (lasers, F/1 lens, and relay lens) which consist of the new optical adjustment system.

2.1 New optical adjustment method

At the start of the developmental stage of FITE, we employed a classical Hartmann test for the evaluation and adjustment of the interferometer optics (Kato et al., 2009). In this test, we used a Hartmann plate that consists of a set of small holes equally spaced in the two-dimensional directions. From the spot positions of the in- and out-focus, the convergence at the best position was derived. The displacement from the optical axis of each beam indicated the accuracy of the optical adjustment. However, we cannot acquire the result in real-time because this method requires several shots of images taken at different positions for the Hartmann analysis. Therefore, this method was not so efficient.

In order to improve the efficiency, we studied two new components, a measurement device with a laser interferometer and a Shack-Hartmann wave front sensor, substituting them for the classical Hartmann test. We adopted the latter because the laser interferometer device is incapable of performing simultaneous measurements from the two mirrors and then cannot detect any shifts of the wavelength between the two mirrors. Moreover, the coherent length of the device is not usually sufficient to measure long optical path lengths (4-m in this case).

On the other hand, the Shack-Hartmann wave front sensor can detect just the wavefront error. In principle, we can make adjustments to the optical system by monitoring this wavefront error of the two beams simultaneously. In this subsection, we describe a new method to perform a simultaneous wavefront analysis of the two beams by using standard wavefront sensors, which are generally used for adaptive optics systems (Wizinowich et

al., 2006). The simultaneous analysis will make the optical adjustment of the two off-axis parabolas easier and more efficient.

To demonstrate this new method, we performed laboratory tests with a prototype system. To switch the measurement mode between the two beams and single beam, we used an extractable beam expander. Section 2.1.1 describes the accuracies of the optical adjustment required by the FITE observation. Section 2.1.2 describes the optical adjustment sequence of the two off-axis parabolas of FITE with a wavefront sensor. Section 2.1.3 describes the optical system and individual roles of the components that are used for the adjustments. In section 2.1.4, the results of the laboratory experiments conducted for demonstration purposes are explained.

2.1.1 Accuracy requirement

The required accuracy for the optical alignment of the two parabolas is determined for the coherence at a wavelength of lambda = 25 um, which is in a range of the mid-infrared band of FITE (Kohyama et al. 2009, Kato et al. 2009). Table 1 lists the accuracies in detail. The latest information of the accuracy requirement for FITE is given in Section 2.3.1.

Table. 1. Accuracy requirement. The latest information of the accuracy requirement for FITE is given in Section 2.3.1.

Image Quality	2.2 arcsec
Prallelism of the Two Beams	11.6 arcsec
Focus Disagreement of the Two Parabolas along Optical Axis	80 μm

2.1.2 Adjustment sequence

The adjustment sequence of the two off-axis parabolic mirrors devised are as following.

1. To determine the input focus position of the cryostat with respect to the output focus position of the cryostat.
   (a) The optical adjustment device is mounted with a spherical reference mirror at the input focus part of the cryostat. We ensure that the curvature center of the

reference spherical mirror coincides with the input focus of the cryostat by illuminating from the output focus part of the cryostat.

(b) Next, we do not need to refer to the output focus, because the curvature center of the spherical reference mirror can be treated as the reference.

2. Make the focus of the adjustment device coincide with the curvature center of the spherical mirror.

(a) Set two flat mirrors to reflect the downward beam in the direction that is horizontal to the wavefront sensor.

(b) Make the alignment of the internal laser light of the adjustment device coincide with the reference spherical mirror.

(c) Remove the reference spherical mirror.

3. Mount the cryostat and the adjustment system on the interferometer optics.

(a) Adjust the two parabolas by using the auto-collimation method.

4. Completed.

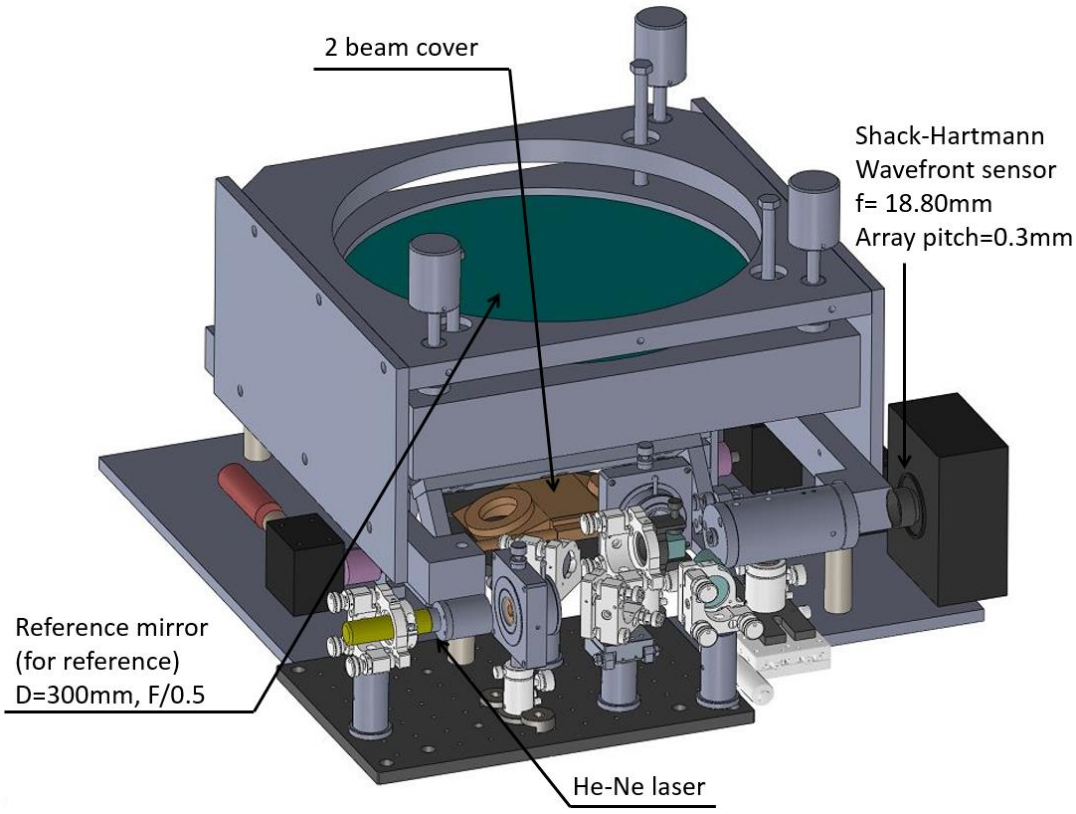

Fig. 2.1 Model of Optical Adjustment device for FITE

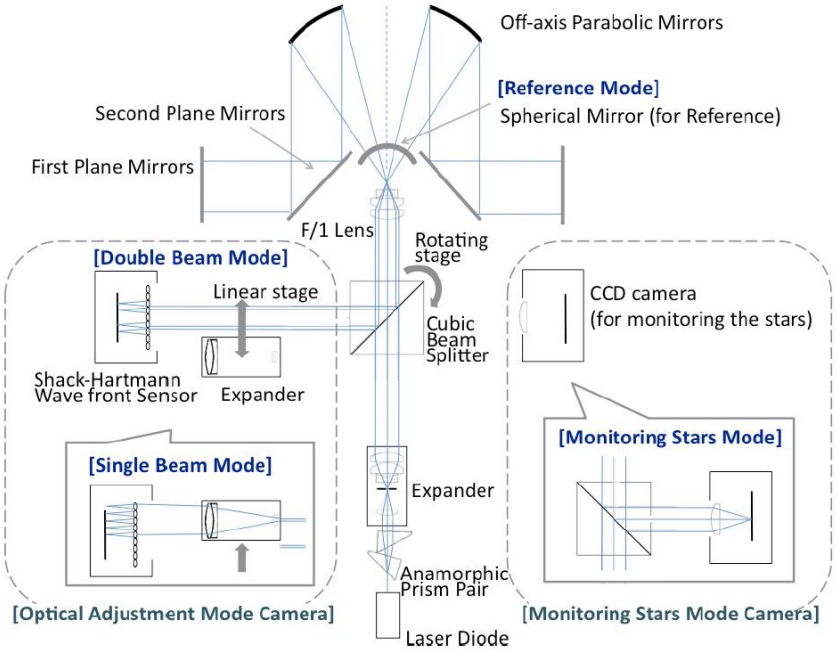

Fig. 2.2 Schematic diagram of the optical adjustment system. This figure shows four different configurations corresponding to individual measurement modes: reference mode, single beam mode, two-beam mode, and monitoring star mode. The reference mirror is used for the reference mode. After taking reference images, this reference mirror is removed and the off-axis parabola mirrors are tested. In the optical adjustment mode, the two beams from the two off-axis parabola mirrors are adjusted with the reference mirror. Finally, this optical adjustment system is employed as a part of the monitoring stars system.

2.1.3 Optical adjustment device

The model of FITE optical adjustment device is shown in Figure 2.1 and the schematic diagram of the optical adjustment system is shown in Fig. 2.2. This device is mounted on the top of the cryostat in which the far-infrared array sensor, mid-infrared array sensor, and the cold relay optics are installed. The structural frame of the interferometer is a box-type one made of aluminum-honeycomb carbon-fiber-reinforced plastic (CFRP) sandwich panels. Therefore, the stiffness of the structure is maintained only when the box is closed. Therefore, the adjustment device can be operated from the outside even when the box is closed. To realize this procedure, two independent CCD cameras are used for adjustments.

The adjustment device is composed mainly of a laser diode light source, a cubic beam splitter mounted on a rotation stage, a converging and dispersing composite lens system (F/1), and the reference spherical mirror (the radius of both curvature and diameter is 300-mm). The cubic beam splitter introduces the light from the reference mirror and the off-axis mirrors to the CCD camera of the wavefront sensor. By rotating the splitter by 90 degrees, the light is switched to the other CCD camera that is used to monitor the stars during observation. Hence, both CCD cameras are used. The first one is the sensor of wavefront detection that uses a micro-lens array to cover the entire array area. In front of this CCD, six times beam expander can be inserted using a linear stage. When this expander is inserted, the wave front pattern of the individual beam can be measured in detail. When extracted, both wave front patterns of the two beams can be measured simultaneously. The second CCD camera is used for a monitoring stars during the observation, and it detects stars for the rough altitude determination of the telescope.

2.1.4 Laboratory test of new optical adjustment system

We constructed a test model of the FITE optical adjustment device and conducted laboratory tests to demonstrate its functionality and performance. We performed two tests. The first one involved checking the fundamental functions, and the other one involved checking the two modes of wave front sensing, that is, single beam measurement and two simultaneous beam measurements, as described in the previous section. Wavefront sensing with the micro-lens array generally requires the use of a precise reference mirror before or after the measurement. The reference mirror is spherical, D = 300 mm, R = 300

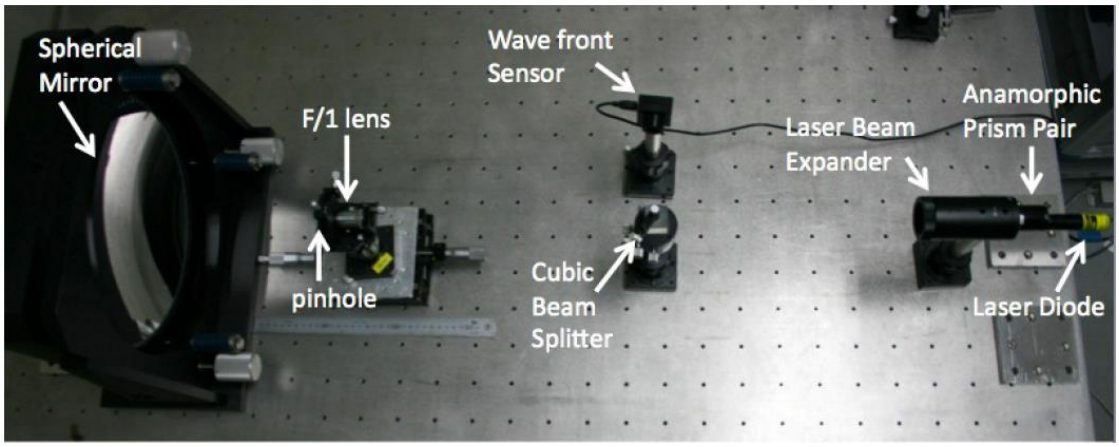

Fig. 2.3 Laboratory measurement configuration by using the reference spherical mirror and the wavefront sensor.

mm, and f = 150 mm (paraxial approximation). Fig. 2.3 shows the test configuration in the optical stage. The light from a laser diode is deformed to a circular beam of 4 mm with an anamorphic prism pair and is expanded by a factor of 4 with a beam expander. The resultant beam diameter is 16 mm. After being reflected with a cubic beam splitter, the beam is converged into a small pinhole and diverged out as an F/1 beam.

The main purpose of this study was to investigate the switching between the two wavefront sensing modes described in the previous section. The optical components were set as shown in Fig. 2.4. The light from the laser diode source is enlarged by the beam expander and is reflected to a small lens. The lens converges the beam, and then diverges into an F/5 beam. A small flat mirror reflects the beam to an accurate parabolic mirror (D = 150 mm, f = 1200 mm). Using the auto-collimation method, the returned beam, which was split by a cubic beam splitter, is introduced to the wave front sensor. This configuration realizes a test model of the actual FITE adjustment device. Fig. 2.4 show the test image in the single beam mode and that in the two-beam simultaneous mode. In the case of the single beam, a small part of the beam is lost because of the FOV of the CCD cameras. However, the analysis was successfully conducted with only the unblocked part of the beam.

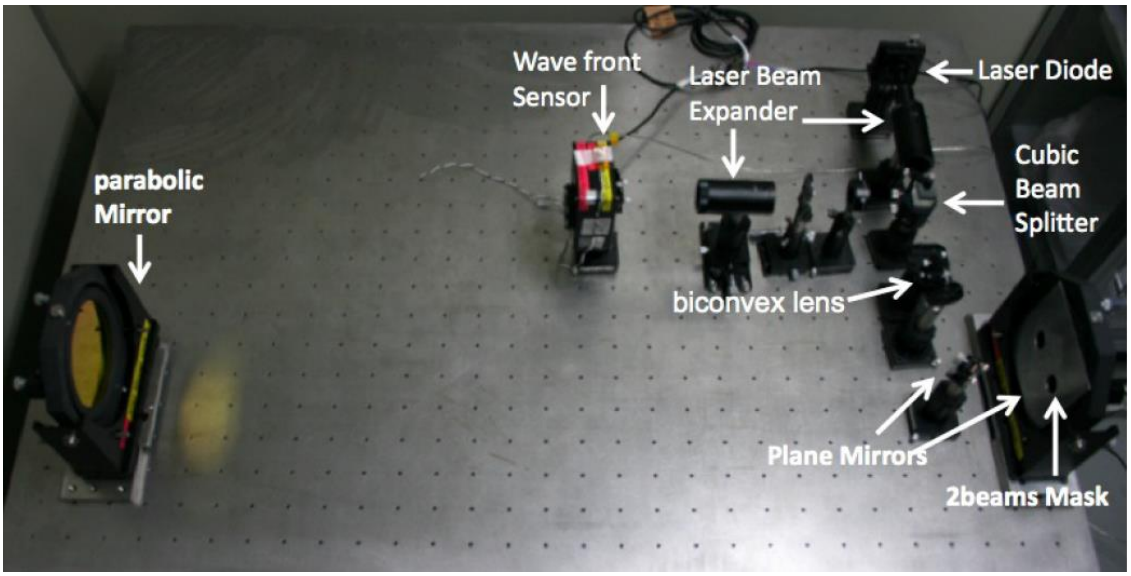

Fig. 2.4 Test configuration of the tw0-beam simultaneous mode and single beam mode.

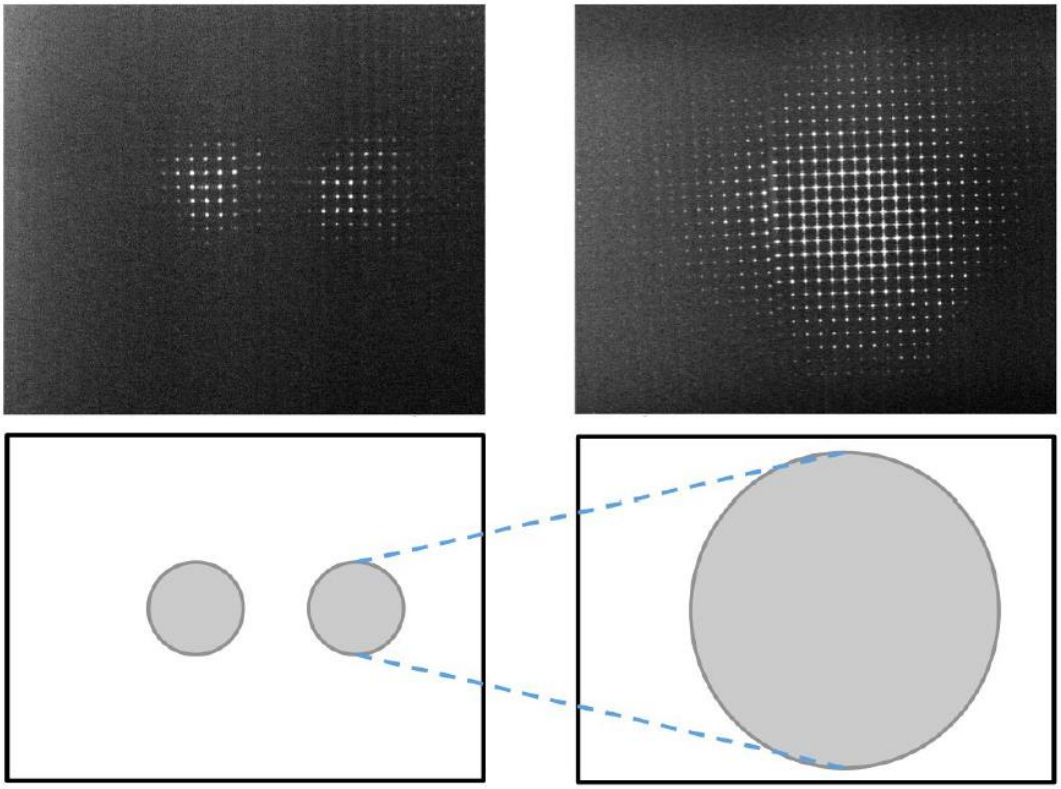

Fig. 2.5 Test image in the single beam mode and that in the two-beam simultaneous mode. Upper left: Image in the two-beam simultaneous beam mode (with the beam expander). Upper right; Image in the single beam mode (without the beam expander). Bottom: Illustration of the two-beam mode, single beam mode and two-beam mode. Single beam mode is an expansion of one of the two beams.

2.2 Development of new optical adjustment system

We demonstrated in the laboratory a new application of the device having the two operation modes: the single-beam measurement and the two-beam simultaneous measurement in Section 2.1 (Sasaki et al., 2012). We can now derive the degree of adjustment of the interferometer optics from each shot of the Shack-Hartmann wavefront sensor. In this subsection, we designed and constructed a new optical adjustment system for FITE. Fig. 2.6 shows the schematic of the new optical adjustment system, while Fig. 2.7 shows the actual instrument based on the schematic diagram. The requirement for the accuracy of the optical alignment, which is determined by the coherence at $\lambda = 25$ um, is already mentioned in the previous section (see Table 1). The focus disagreement of the two parabolas along the optical axis and the parallelism of the two beams are adjusted during flight by remote control from the ground. The adjustment of the optical system is required so that the image quality is smaller than 1.1 arcsecond in radius before launch. The new optical adjustment system can measure and evaluate the image quality of the FITE interferometer. We can use this new optical adjustment system at high altitudes

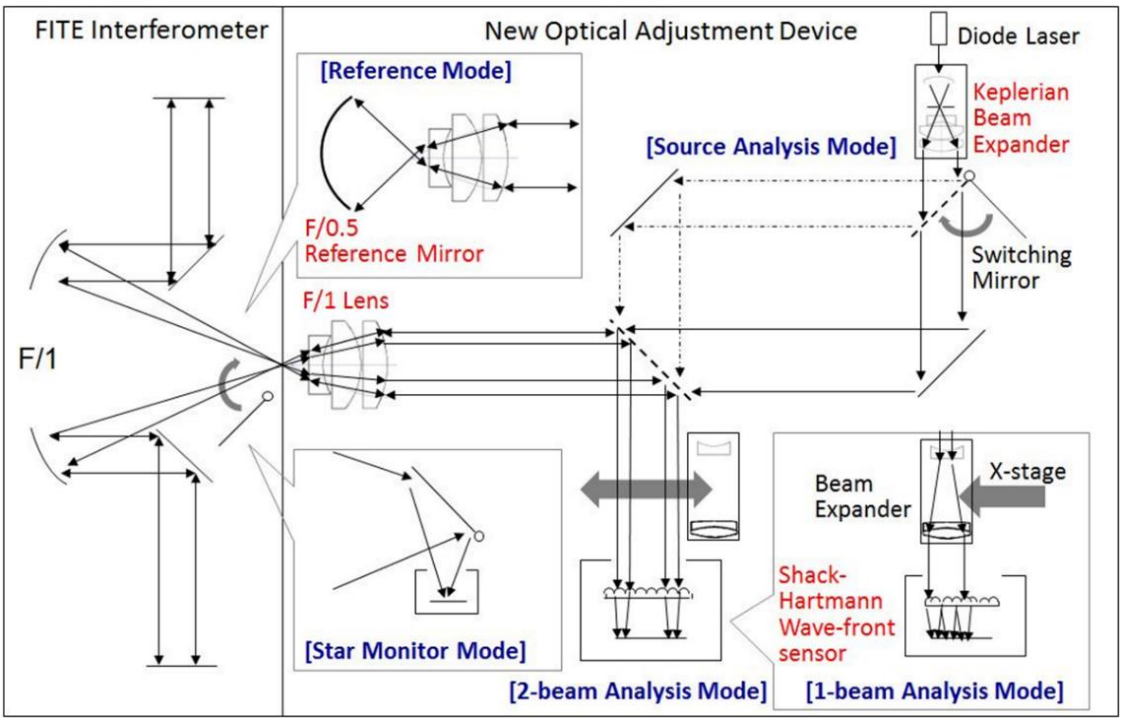

Fig. 2.6 Schematic of the optical adjustment system for FITE. The red words show five different configurations corresponding to individual measurement modes. The blue words show these modes.

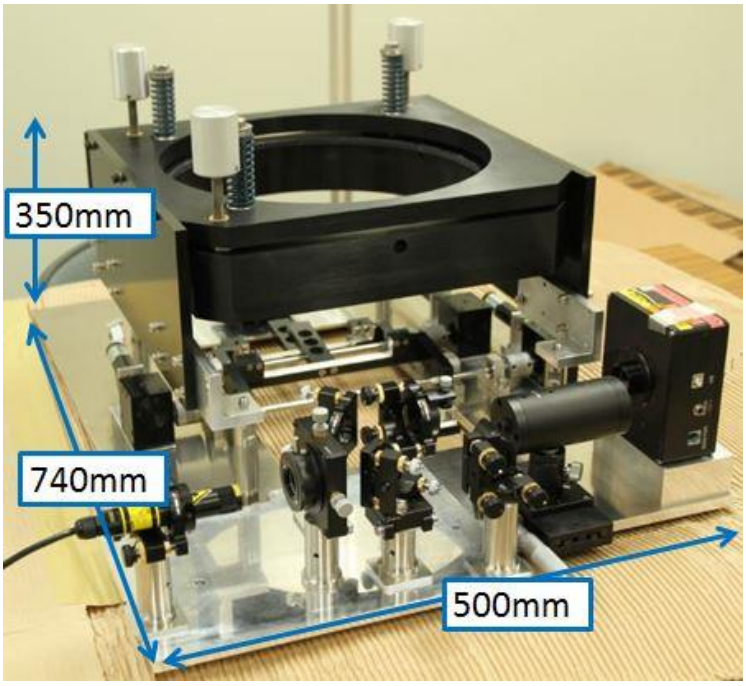

Fig. 2.7 Instrument of new optical adjustment system for FITE. The mass of this adjustment system is 35 kg.

during balloon flight in principle. However, we will use it only before launch at the first flight. Therefore, we do not consider the environmental condition at high altitudes (30 km).

2.2.1 Optical device fabrication

To develop this new optical adjustment system, we need the following optical devices, which we designed and constructed.

A. F/1 collimator lens

The F ratio of the two off-axis parabolic mirrors is almost F/1. Therefore, to simultaneously measure the two mirror surfaces, we require an F/1 collimator lens. According to the requirement of the FITE interferometer, we need to use a collimator lens that has an image quality of less than 1.1 arcsecond. However, such a lens could not be found in ready-made products having a sufficient accuracy of the FITE optics at 635 nm. Thus, we designed a combined F/1 lens with a suitable performance by using ready-made lens products. We designed and manufactured lens holders, as

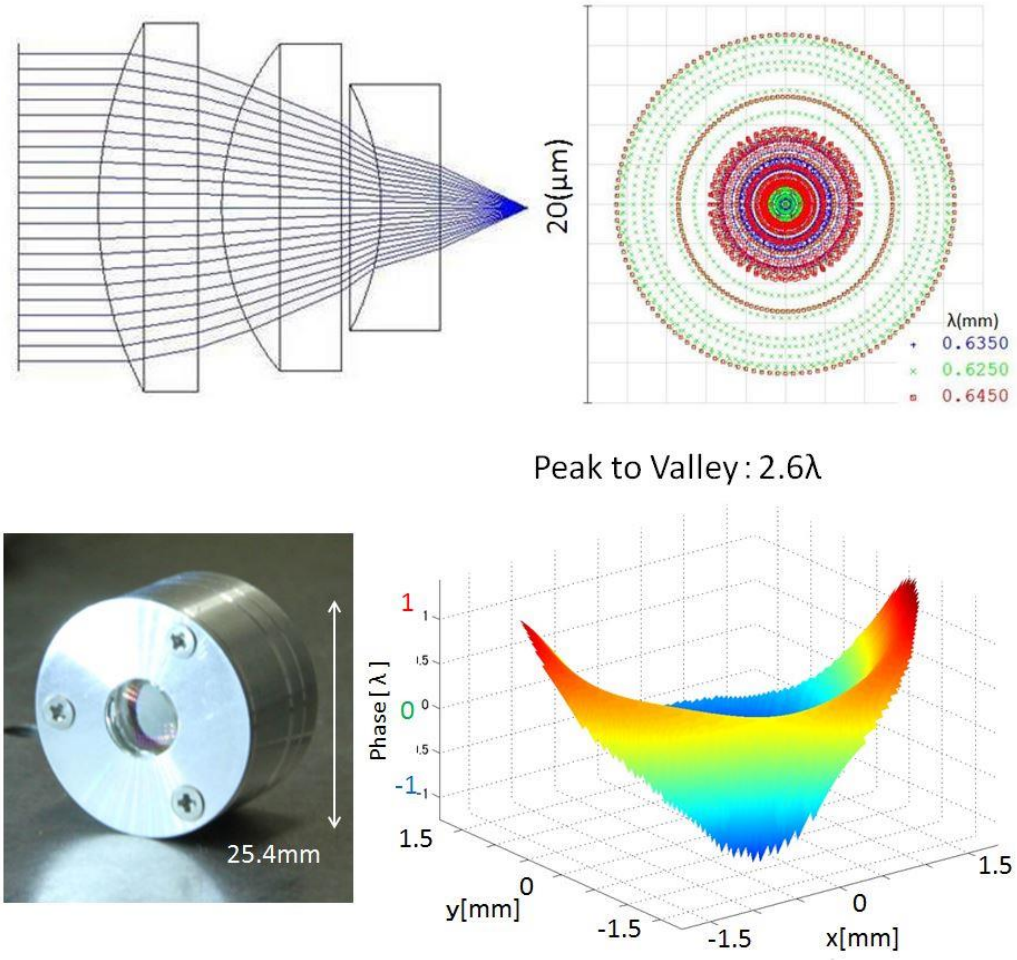

Fig. 2.8 F/1 collimator lens. Top left: F/1 collimator lens 3D layout. This lens consists of three ready-made lens products. Top right: Image quality at focal plane of this collimator lens. Bottom left: picture of assembled lens. Bottom right: Test data of the collimator lens using Shack-Hartmann wavefront sensor. This data shows that the test collimator lens acquired the required accuracy of the FITE interferometer system.

shown in Fig. 2.8, after which we tested them. Using an optical software, Zemax OpticStudio®, we made an inverse beam simulation, and found that the image quality of 0.55 arcsecond in radius corresponds to the wavefront accuracy of approximately 4 λ at 635 nm. In other words, a collimator lens having an image quality of 0.55 arcsecond in radius satisfies the requirement of the FITE interferometer (1.1 arcsecond in radius). The light from the diode laser is put on the diffuser. A part of the diffused light passes through a pinhole with a 5-μm diameter to make a diverging point source. The pinhole is placed at the focus of the collimator

lens. Therefore, the light beam arriving at the collimator lens from the focus becomes a collimated beam after passing through the collimator lens. We can determine the alignment accuracy of the lens system by measuring the wavefront error of the beam. On the basis of the laboratory test results, we demonstrated that they satisfied the required accuracy (see Table 1). The test result shows that the collimator lens achieved a p-v accuracy of −2.6λ.

B. Keplarian laser beam expander

We also constructed a Keplarian laser beam expander for the same reason (shown in Fig. 2.9). It consists of five commercial lenses. We measured the wavefront error of the output beam of the laser beam expander to which the laser beam is introduced. The diameter of the pinhole in the expander is 5 μm. The test result shows that the Keplarian laser beam expander achieved the p–v accuracy of 1.8 λ, as shown in Fig. 2.9.

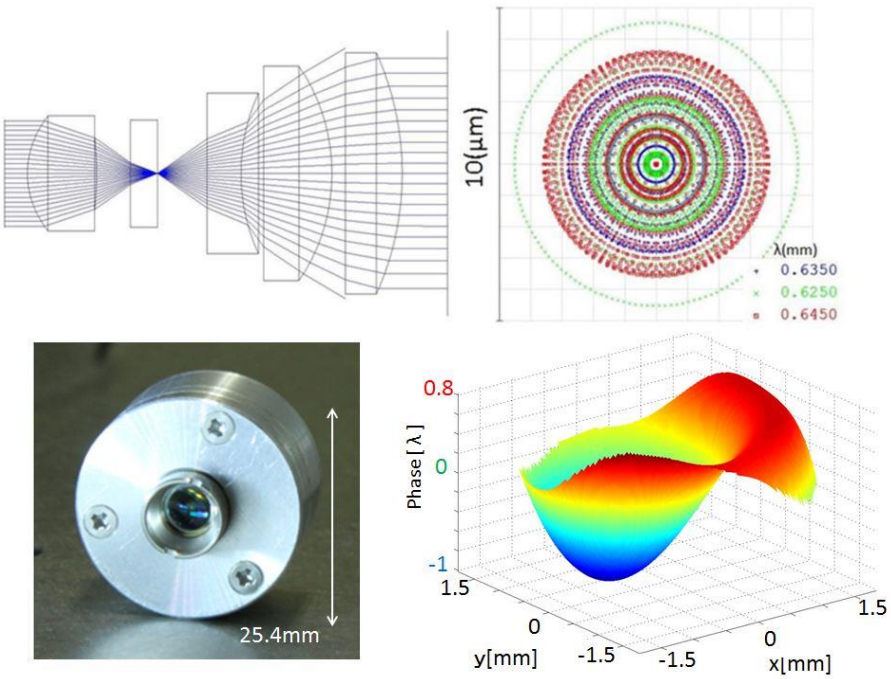

Fig. 2.9 Keplarian laser beam expander. Top left: Keplarian laser beam expander lens 3D layout. This lens consists of five ready-made lens products and a pinhole of φ 5μm. Top right: Image quality at focal plane of this lens. Bottom left: picture of assembled lens with holder. Down right: Wavefront error data for the Keplarian laser beam expander using Shack–Hartmann wavefront sensor. This data shows that the test keplarian laser beam expander lens has a 1.8-λ peak-to-valley value.

C. Shack-Hartmann wavefront sensor

The new optical adjustment system for FITE enables us to measure not only one beam but also two beams simultaneously. Ready-made Shack-Hartmann wavefront sensors are not able to simultaneously measure the two beams. Therefore, we constructed a Shack-Hartmann sensor for FITE and developed software in C that simultaneously analyzes two wavefront error maps. The Shack-Hartmann wavefront sensor is shown in Fig. 2.10. The CCD array size is 13.8 mm × 9.8 mm. To cover the CCD array, we put in two micro lens arrays and set its size to 20 mm × 10 mm. In addition, we selected micro lens array specification suited for the FITE optical adjustment system. We have constructed a test model of the optical adjustment system of FITE and carried out laboratory tests in order to demonstrate the performance of lens array. Finally, we chose one which has focal length of 18.8 mm and micro lens array diameter of 0.5 mm.

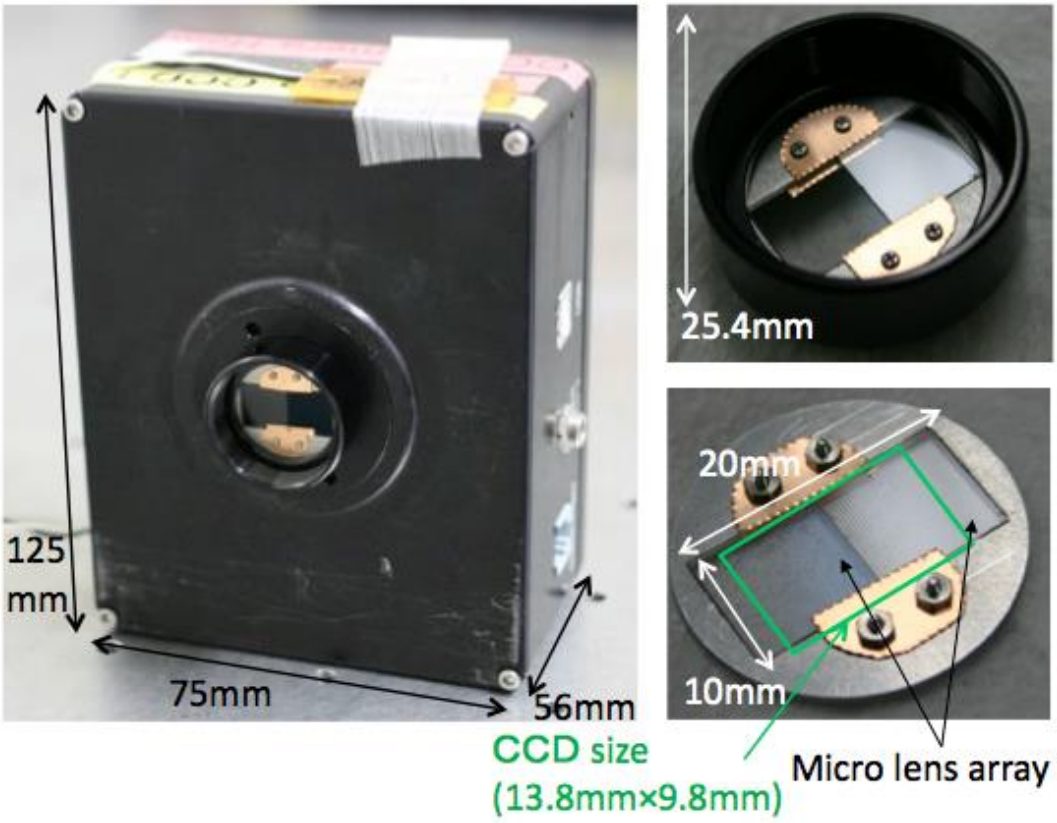

Fig. 2.10 Shack-Hartmann Wavefront sensor. Top left: Left: Picture of Shack-Hartmann wavefront sensor for new optical adjustment system. Top right: Close-up photo of the lens holder. Bottom right: Lens parts. This Shack-Hartmann wavefront sensor uses two micro lens arrays and is of size 20 mm × 10 mm. The CCD array size

D. Reference Mirror

Finally, we require a high-quality reference mirror for reference purposes. Because the total F ratio of the FITE collecting optics including two off axis parabolic mirrors is almost 1, we designed and manufactured an F/0.5 spherical reference mirror having a diameter of 300 mm. This mirror was manufactured with optical polishing. The accuracy of the mirror was measured with the classical knife-edge method, and the result was roughly λ/15 at 555 nm, which is sufficiently accurate for FITE. The mirror and its information are shown in Fig. 2.11.

Effective diameter	300mm
Focal length f	150mm
Center of curvature R	300mm
Mirror accuracy	λ/15
Material	PYREX
Coating	Al+SiO
IK Giken Co., Ltd.	

Fig. 2.11 Reference Mirror. Left: Picture of spherical reference mirror. Right: Table of reference mirror information. The diameter of the reference mirror is 300 mm, and the mirror accuracy is λ/15 at 555 nm.

2.3 Optical adjustment results of FITE interferometer

This subsection describes the results obtained from the use of the interferometer adjustment method for FITE. Towards the JAXA Australia balloon experiment campaign 2018 held at the Alice Springs balloon base, interferometer adjustment was carried out in the laboratory before shipping. Section 2.3.1 explains the required accuracies of the off-axis parabolic mirrors with the interferometer adjustment system. The modification of the method and procedure for the interferometer adjustment is described in Section 2.3.2. Section 2.3.3 describes the interferometer adjustment's result. Results will be discussed in Conclusion.

2.3.1 Accuracy requirement

Table 2. Accuracy requirements of FITE interferometer optics for 155 μm

Item	Requirements
i. Wavefront error (in peak-to-valley)	< 38.8 μm See Eq. (1)
ii. Image quality (Hartmann constant)	< 33 arcsecs See Eq. (2)
iii. Optical path difference between the two beams	< 250 μm See Eq. (3)

In order to detect the interference fringes at 155 μm, the alignment of the FITE interferometer optics must be achieved with enough accuracy (see Table 2 for specifications). The accuracy requirement of the FITE interferometer optics is divided into two parts: adjustment of the two off-axis parabolic mirrors and adjustment of the four plane mirrors. The former part, the accuracy requirements for the positions and attitudes of the two off-axis parabolic mirrors, is described below. These two off-axis parabolic mirrors are adjusted by using the interferometer adjustment system with the autocollimation method. The latter part, the positions and attitudes of the four plane mirrors, is beyond the scope of this thesis and is controlled with the attitude control system of the FITE payload.

Table 2 shows the required accuracies for the two off-axis parabolic mirrors. The items to be adjusted before launch on the ground are (i) the peak-to-valley wavefront error for each off-axis parabolic mirror, and (ii) the Hartmann constant, where the two off-axis parabolic mirrors are regarded as two parts of a single parabolic mirror. The third item, the optical path difference between two beams, should be adjusted during flight by using celestial point sources. The observation wavelength is assumed to be 155 μm. Details of these required accuracies are as follows:

i. Wavefront error (in peak-to-valley)

Distortion of the wavefront may degrade interference efficiency. In order to efficiently detect the interference fringe pattern, the phase difference error, called the peak-to-valley wavefront error, adjusted within $\pi/2 = 1/4$ of a wavelength of λ. This requirement is represented by

$$\text{Wavefront error (p} - \text{v)} < \frac{\lambda}{4} = \frac{155\ \mu m}{4} = 38.75\ \mu m \quad (1)$$

.

ii. Image Quality (Hartman constant)

Consider the case that two beams overlap on a focal plane and then interference fringes are generated. We set a requirement that the intensity difference between the central peak of the interference fringes (optical path difference is zero) and the first valley (optical path difference is $\lambda/2$) is satisfied to have a sharpness of ≥ 0.6 compared to the central peak intensity with no aberration. The reason for setting sharpness to this degree is because the S/N of the interference fringes does not deteriorate. Since the interferometer adjustment test is carried out with visible light, it is necessary to know the relationship between the aberration measured by visible light and the sharpness at 155 μm. Therefore, the relationship was determined as follows using the optical analysis software Zemax OpticStudio®. It was assumed that that, in the case of the FITE interferometer optics, the degradation to a sharpness of 0.6 was only due to the shift in the optical axis direction (i.e., defocus). In the previous case, the RMS radius was 711 μm when two off-axis parabolic mirrors were regarded as part of a single parabolic mirror. In addition, the ratio of the RMS radius to the radius of the airy disk was 2.82. Hence, the ratio of the imaging performance (RMS radius), determined by geometric optics, to the airy disk radius, determined by wave optics, was approximately 1:3. In the following, the rms radius was calculated as 1/3 of the airy disk radius size. Since the airy disk radius at 155 μm was $1.22 \cdot (\mathrm{F}/4) \cdot 155\ \mu\mathrm{m} = 756.4\ \mu\mathrm{m}$, where F/4 represents the F ratio of 4, the RMS radius was estimated to be about 250 μm, and then the diameter was done to be about 500 μm.

There are modes other than defocusing for which sharpness is degraded, but the ratio of the RMS radius and the airy disk radius is approximately the same. When the

Hartmann constant (T_{HM}) of two off-axis parabolic mirrors is regarded as part of a single parabolic mirror, the following equation is applied:

$$THM = \frac{RMS\ radius}{focal\ length} \sim \frac{250\ \mu m}{1560.97\ mm} \sim 33 \text{ arcsecs.} \qquad (2)$$

where the *focal length* of the off-axis parabolic mirror is 1560.97 mm. This result means that, even if two beams do not overlap geometrically on the image plane, airy disks will overlap, as in the case when the Hartmann constant is $\leq$ 33 arcsecs. Hence, it is expected that the sharpness of interference fringes will be $\geq$ 0.6 in the case where the Hartmann constant is $\leq$ 33 arcsecs.

iii. Optical path difference

The optical path difference is required to be smaller than one radian phase difference, i.e., the optical path difference is $\leq$ the coherence length. The coherence length (d) is determined by the following equation:

$$d = \frac{\lambda^2}{\pi \cdot \Delta\lambda} = \frac{(155\ \mu m)^2}{\pi\ \cdot\ 30\ \mu m} = 255\ \mu m \qquad (3)$$

.

where the bandwidth ($\Delta\lambda$) of FITE is 30 μm at 155 μm. Hence, if the optical path difference between the two beams is adjusted within 255 μm to keep the phase difference less than $<$ 1 radian (about 60 degrees), the interference fringes are then generated on the image plane. In order to adjust the optical path difference, the position of the secondary plane mirror is adjusted stepwise by 250 μm during observation. As a result, the observed data must include the point of the optical path difference of ±125 μm. Through this operation, visibility can be measured at two or more points.

2.3.2 Modifying elements of the interferometer adjustment system and the adjustment procedure

The interferometer adjustment system for FITE was designed and developed per the required accuracies described in Section 2.3.1. A diagram of the FITE optical system is shown in Fig. 1.5. The FITE optical system has four optical sub-systems: the FITE interferometer optics used for collecting light from a celestial object, the mirror adjustment instrument used for adjustment, the sensor optics (Kohyama et al., 2008) used for astronomical observation, and the star monitor camera used for the attitude control of the FITE gondola. These optical systems are part of the in-flight equipment. However, the mirror adjustment instrument is only used before launch and not used during flight. Each optical system is switched by inserting and removing two switching mirrors placed in front of the first focal point.

The principle of the mirror adjustment method and the mirror adjustment instrument for FITE is described in Sasaki et al. (2012) and (2014). The interferometer adjustment system was further modified for the first flight. In the following, three modifications of the newly developed interferometer adjustment system (secondary model) are described.

A Speed up of the Shack-Hartmann Wavefront sensor

The imaging device of the Shack-Hartmann wavefront sensor was changed to a CMOS imaging device manufactured by iDS (model number: UI-3180CP-M-GL Rev. 2). As a result, although the CCD used in the primary model had the shortest exposure speed of 0.09 seconds, it became 0.025 seconds after the change. Hence, the influence of vibration at the time of interferometer adjustment was reduced without changing the structure of the FITE gondola. The telescope box of the FITE with the interferometer adjustment system was connected to the FITE gondola-frame by bearings. At the time of the interferometer adjustment test, the bearing was fixed so as not to rotate. However, it was unstable compared to the time of the interferometer adjustment test on the optical board in the laboratory. Although the analysis was possible even with the primary model device, the impact was reduced because of the reduction in the wavefront sensor exposure time.

B Changing the light source and F/1 collimator lens

The light source was changed from a diode laser to a He-Ne gas laser. Along with this change, the F/1 compound lens was also changed to a ready-made F/1 collimator lens (manufactured by Edmund optics, model number: #87-988), optimized for a wavelength used in the He-Ne gas laser.

Due to the bandwidth of the diode laser (633 nm ±10 nm), the imaging performance of the FITE interferometer optics was degraded by the chromatic aberrations of the refracting optics (a beam expander and the F/1 compound lens) in the interferometer adjustment system. In order to satisfy the required imaging performance of the primary model (Hartmann constant 1 arcsec, RMS radius 7 μm), the F/1 compound lens was assembled and used (Sasaki et al., 2014). However, even with the F/1 compound lens, the required imaging performance was marginally satisfied since the F/1 compound lens was assembled as three lenses, and it was very difficult to coincide the relative installation accuracy of each lens. The ready-made F/1 collimator lens is a single lens. Therefore, lens installation became easy. Also its imaging performance, by knife edge measurement, was < 5 μm at the wavelength of the He-Ne gas laser, which satisfied the required imaging performance.

C Inserting the relay lens

In order to re-image the pupil at the microlens array position of the Shack-Hartmann wavefront sensor, a relay lens was placed in front of the sensor. As a result, even if each off-axis parabolic mirror largely deviated from its ideal state, the position of the pupil did not move so much, which made the measurement possible. This is a common use of the Shack-Hartmann wavefront sensor.

In the primary model of the mirror adjustment instrument, there was a beam expander with a magnification of 4× in front of the Shack-Hartmann wavefront sensor (Sasaki et al, 2014). When the beam expander was inserted on the optical axis, each beam from each off-axis parabolic mirror was expanded and incident on the Shack-Hartmann wavefront sensor. Thanks to this expansion, fourth-order or higher order aberration terms were measured when the peak-to-valley error of each beam was measured. However, since it is known that the accuracy of two off-axis parabolic mirrors itself is sufficiently high, the aberration was mainly due to installation error. Since the installation error was only a low-order aberration term, there was no need to expand

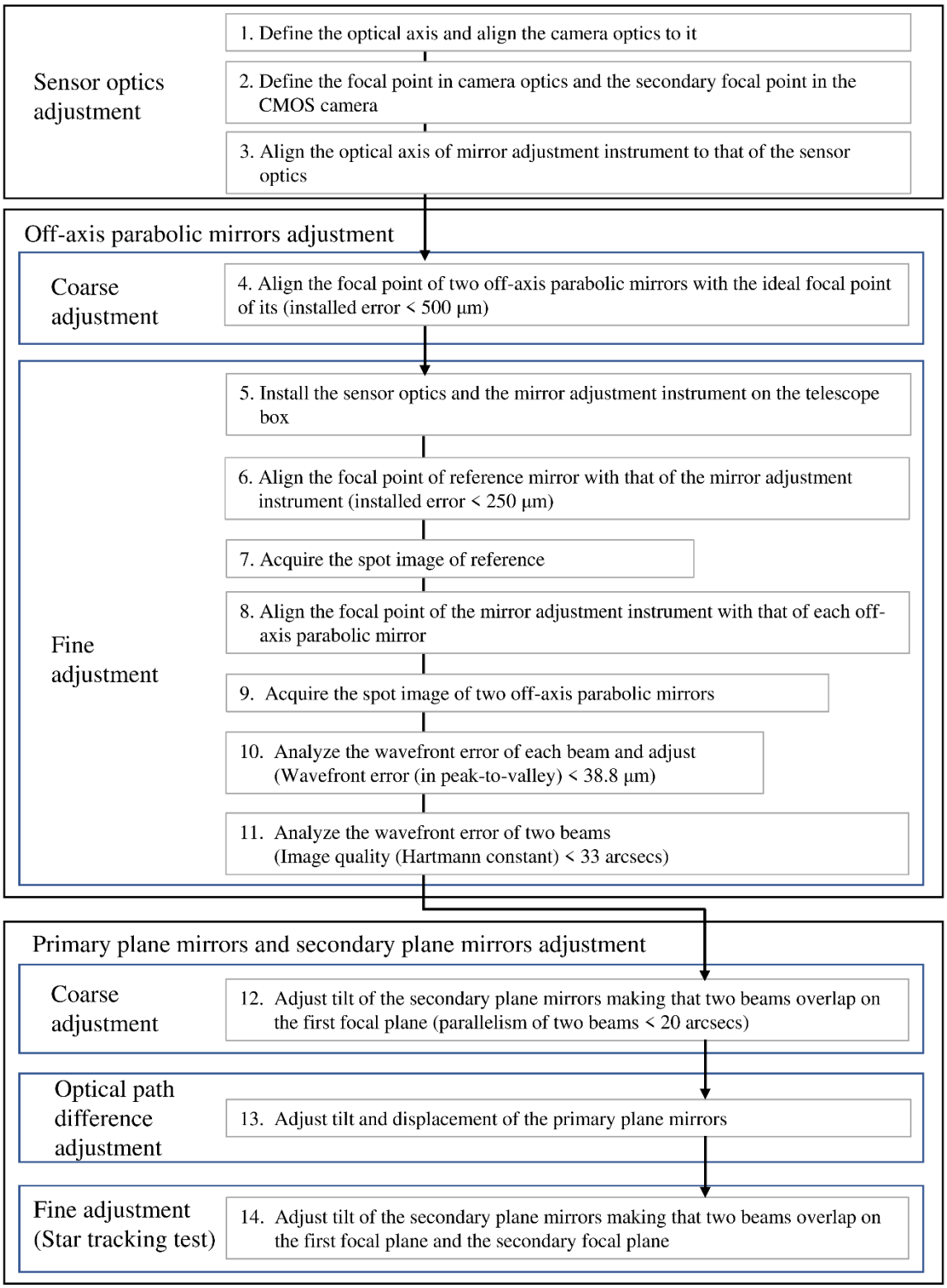

Fig. 2.12 Adjustment procedure of the FITE optical system.

each beam. Conclusively, we decided to commit to a low-order aberration analysis of up to the third order. In this case, the unexpanded beam size was 7 × 7 points, and this was sufficient for aberration analysis.

To achieve the required accuracies in Section 2.3.1, the interferometer adjustment test was carried out. The procedure for the FITE optical system is shown in Fig. 2.12. We aligned the system so that the light reflected on the optical components could not go back into the laser. Hence, the laser problems were not occurred. In this subsection, we describe the results of the interferometer adjustment shown in steps 4 to 11. The adjustment of each required accuracy described in Section 2.3.1 was carried out in steps 10, 11, and 13.

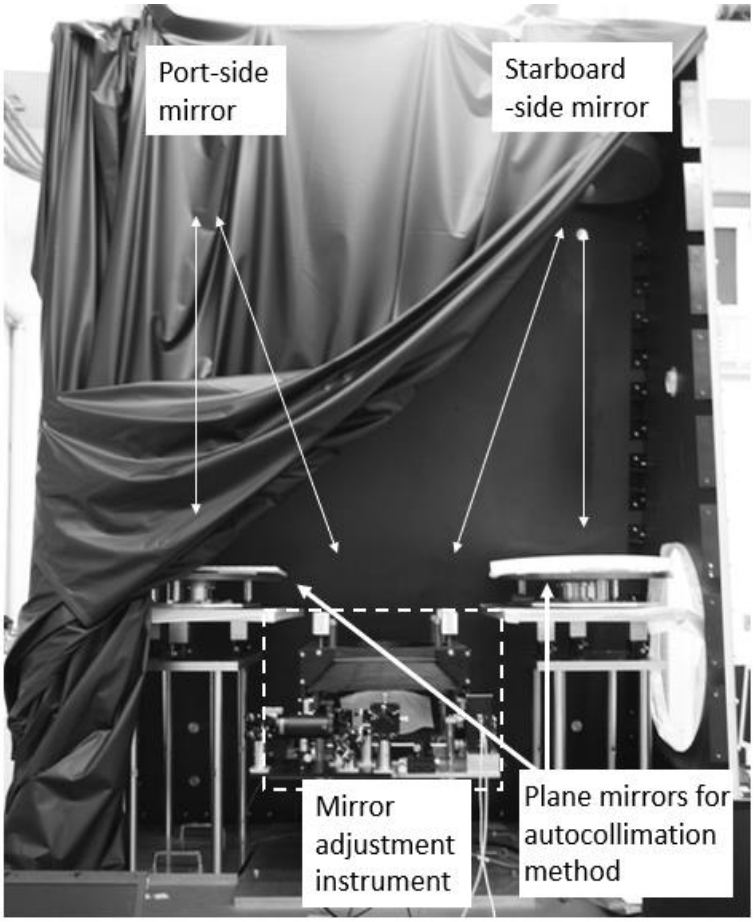

Fig. 2.13 Setup of the interferometer adjustment test carried out before shipping to Australia. (top) Two off-axis parabolic mirrors, port-side mirror and starboard-side mirror, which used for collecting light from a celestial object are corresponded to the FITE interferometer optics in Fig. 1.5. (bottom) The part surrounded by the dotted line is corresponded to the mirror adjustment instrument in Fig. 1.5. In this Figure, two plane mirrors for autocollimation method were installed at the place of the secondary

2.3.3 Results of the interferometer adjustment

Each off-axis parabolic mirror was adjusted with the interferometer adjustment system for launch in Australia. In this section, we first describe the setup of the adjustment test, then describe results of the tests carried out before shipping and launch.

A Procedure of interferometer adjustment

Fig. 2.13 shows the setup of the interferometer adjustment test carried out before shipping to Australia. The adjustment test was carried out on the granite table. It was carried out using the autocollimation method. As shown in Fig. 1.5 and Fig. 2.13, light from the interferometer adjustment system was reflected by each off-axis parabolic mirror and was made incident back on the system. Subsequently, these two beams were collimated by the F/1 collimator lens (Section 2.3.2). These two collimated beams were detected as a spot image (Fig. 2.14b) in the Shack-Hartmann wavefront sensor. Displacement of these spots was measured from the spot image (Fig. 2.14b) with the reference image (Fig. 2.14a) acquired in advance as a reference. Herewith, the vector map (Fig. 2.14c, Fig. 2.14d, and Fig. 2.14e), which showed wavefront phase error, was acquired from displacement of Fig. 2.14a and Fig. 2.14b spots. Zernike coefficients (the fourth row from left in Table 3) were then calculated with the normalized fringe Zernike polynomial (the third row from left in Table 3). The Zernike coefficient is known to correspond to the Seidel aberration (Lakshminarayanan and Fleck 2011) shown in the first row from left in Table 3. Finally, the aberration generated due to the installation error of each off-axis parabolic mirror was acquired by Zernike coefficients.

Two types of analysis were carried out in the interferometer adjustment system. First, the peak-to-valley wavefront error of each off-axis parabolic mirror (port-side: Fig. 2.14c, starboard-side: Fig. 2.14d) was analyzed. Next, a Hartmann constant regarding the two beams as part of a single parabolic mirror, was analyzed. This analysis corresponded to steps 10 and 11 in Fig. 2.12.

B Results of interferometer adjustment in the laboratory before shipping

Fig. 2.14 shows the data acquired in the interferometer adjustment test carried out before shipping to Australia. The horizontal axis is the baseline direction, and the vertical axis is the normal to the baseline direction. These axes are the same for all

images. Vectors drawn in Fig. 2.14c, 2.14d, and 2.14e are displayed larger than the actual vector for easy viewing. Fig. 2.14c show the data of port-side off-axis parabolic mirror, Fig. 2.14d show the data of the starboard-side off-axis parabolic mirror, and Fig. 2.14e show the data of the two off-axis parabolic mirrors, regarded as part of a single parabolic mirror. Some dark areas seen in Figs. 2.14a and 2.14b show the holding part of the switching mirror (the large square area seen at the upper part of Fig. 2.14a) and the boundary part between the two microlens arrays (the line seen at the center of Fig. 2.14a). These dark areas did not affect the analysis as they were outside the data used as a reference. The dark spots overlapping each beam were the opaque spot where the microlens array was intentionally filled. These dark spots were used to correctly coincide the pupil position of each beam with that of the reference.

Table 3 shows the results of interferometer adjustment using the normalized fringe Zernike polynomial. Peak-to-valley wavefront errors of each off-axis parabolic mirror were 0.77 μm on the port-side and 1.23 μm on the starboard- side. In the higher order aberration terms, measurement error and shape error of the FITE interferometer optics were measured.

The Hartmann constant was 3.38 arcsecs. In these results, installation errors of the two off-axis parabolic mirrors satisfied the required accuracy to detect interference fringes at the mid-infrared wavelength of 25 μm: the peak-to-valley wavefront error of each off-axis parabolic mirror was 12.5 μm, and the Hartmann constant was 5.5 arcsecs.

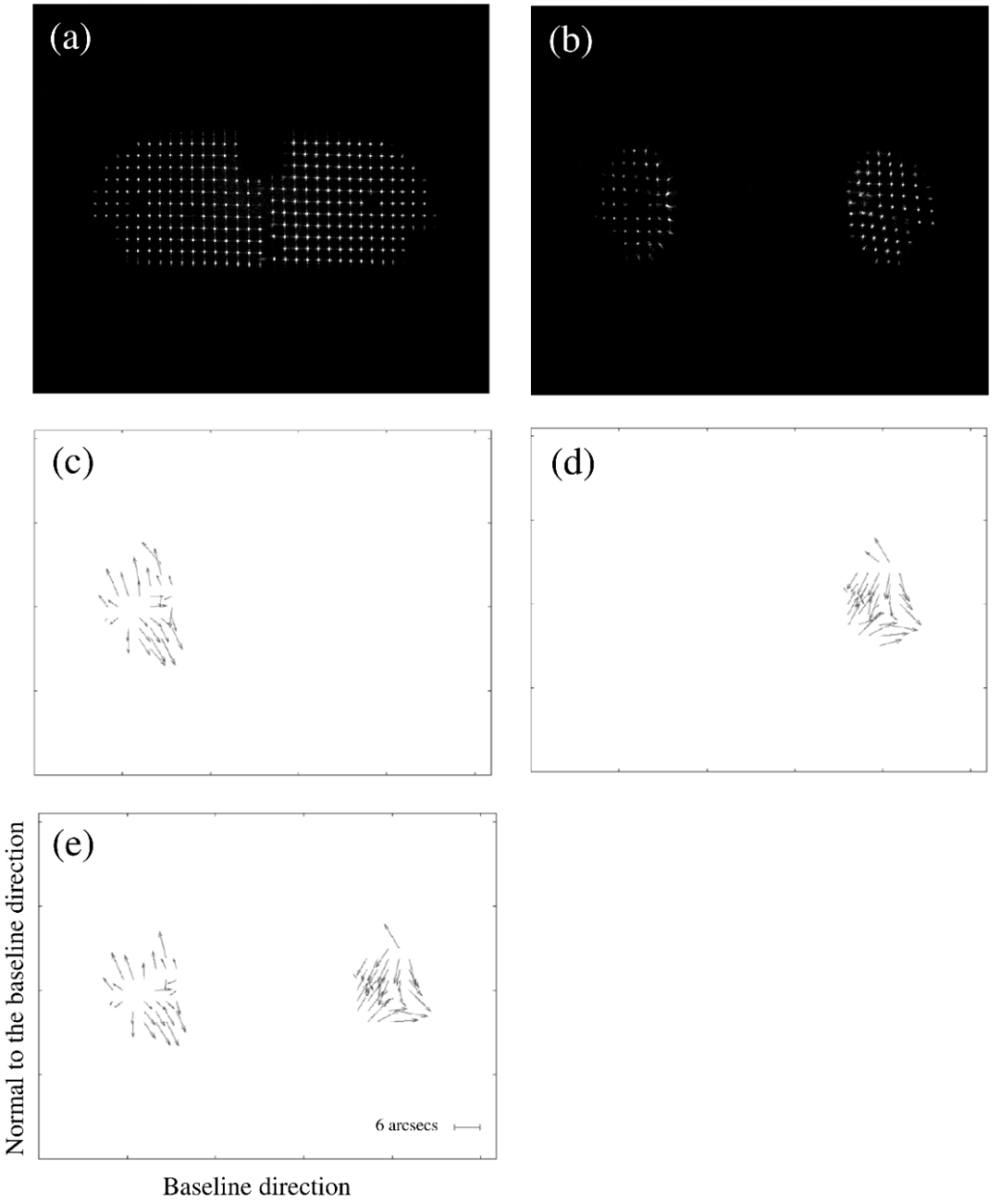

Fig. 2.14 Data acquired in the interferometer adjustment test carried out before shipping to Australia. The horizontal axis is the baseline direction, and the vertical axis is the normal to the baseline direction. These axes are the same for all images. The vectors were acquired from displacement of spots measured from the spot image with the reference image. The vectors are displayed 7 times larger than the actual vector for easy viewing. (a) Spot image of the reference. (b) Spot image of off-axis parabolic mirrors. (c) Vector map acquired from the spot data of the port-side off-axis parabolic mirror and reference. (d) Vector map acquired from the pot data of the starboard-side off-axis parabolic mirror and reference. (e) Vector map acquired from the spot data of two beams and reference. We show the scale of 6 arcsecs with a solid line in panel e.

C Results of interferometer adjustment before launch

Fig. 2.15 shows the data acquired in the interferometer adjustment test carried out on-site before launch. Table 3 shows the analysis results. Peak-to-valley wavefront error of each off-axis parabolic mirror was 1.78 μm on the port-side and 4.99 μm on the starboard-side. The Hartmann constant was 13 arcsecs. With these results, installation errors of the two off-axis parabolic mirrors satisfied the accuracy which is requred to detect the interference fringes at 155 μm (Table 2).

However, residuals remained in the Zernike coefficients Z[2] and Z[3] with these results. These residuals were studied by analyzing the optical model of the FITE optical system by using the optical analysis software Zemax OpticStudio®. In this analysis, the parabolic mirror on the optical model were intentionally moved by five degrees of freedom (X-axis tilt, Y-axis tilt and three-axes decenter) to generate installation errors. There was no need to adjust Z-axis tilt. The normalized fringe Zernike polynomial was then expanded in these installation errors, and the Zernike coefficient was calculated. Results using the optical analysis software Zemax OpticStudio® are shown in right side on Table 3.

In these analysis result, the numerical change of the Zernike coefficients with tilt or decenter followed the same ratio. Therefore, it was difficult to distinguish which installation error caused the aberration. These results meant that, if the off-axis parabolic mirror had an aberration due to decenter error, the wavefront phase error could be reduced by inclining the off-axis parabolic mirror. Hence, the interferometer adjustment test was carried out only adjusting the three degrees of freedom: X-axis tilt, Y-axis tilt, and Z-axis decenter.

Tilt errors of the two off-axis parabolic mirrors were calculated by conversion from the analysis results. As a result, the port-side off-axis parabolic mirror was tilted −8.5 arcsecs on the X-axis and −5.5 arcsecs on the Y-axis, while the starboard-side off-axis parabolic mirror was tilted 11.3 arcsecs on the X-axis and −24 arcsecs on the Y-axis. Therefore, the peak-to-valley wavefront error of the analysis results before launch should have been eliminated by adjusting the particular degree of freedom. Considering the Hartmann constant, 13 arcsecs was larger than the results of interferometer adjustment in the laboratory. However, it was easily corrected by merely adjusting the tilt of the plane mirrors without moving the off-axis parabolic mirror. Hence, it could be adjusted to achieve the same accuracies as the results of the interferometer

adjustment in the laboratory. Since results of the interferometer adjustment before launch satisfied the required accuracies at 155 μm, we finished the interferometer adjustment as shown in Table 3.

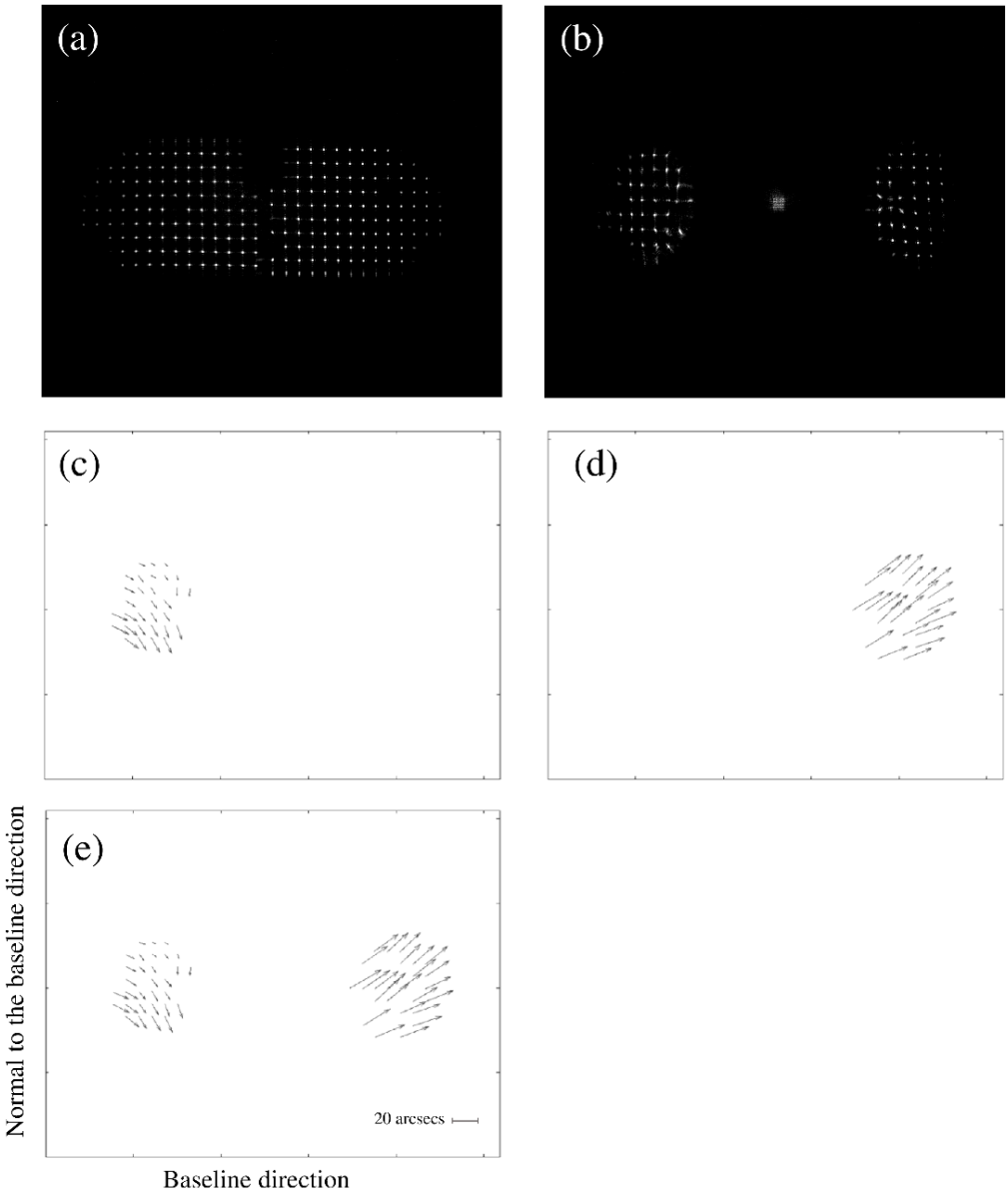

Fig. 2.15 Final adjustment result obtained before launch. Same as Fig. 2.14, except for the scale. We show the scale of 20 arcsecs with a solid line in panel e. This final alignment result is obtained before launch. Compared to the vector scale of 20 seconds in Fig. 2.15e, these results are consistent with the Zemax OpticStudio® analysis results of Table 3.

Table. 3. (Top) Analysis results in the laboratory and before launch (Top right) Analysis results using the optical software Zemax OpticStudio®. (Bottom) Accuracy requirements are same as Table.2. As the result, each off-axis parabolic mirror before the launch has the installation error of the analysis result in Zemax OpticStudio®. In the higher order aberration terms, measurement error and shape error of the FITE interferometer optics were measured. Since the final alignment result satisfied the accuracy requirements, we finished the interferometer adjustment at this state.

Aberration	Surface plot	Normalized fringe Zernike coefficients polar form ($dx^2 \rightarrow rd\theta dr$)	Order	Alignment result in the laboratory before shipping		Final alignment result before launch		Zemax OpticSmdio® analysis result	
				Port [μm]	Starboard [μm]	Port [μm]	Starboard [μm]	Port [arcsecs]	Starboard [arcsecs]
Piston or bias		1	Z[1]	—	—	—	—	—	—
X-tilt		$2\rho\cos\theta$	Z[2]	−0.06	0.57	0.70	3.06	−5.5	−24
Y-tilt		$2\rho\sin\theta$	Z[3]	0.19	−0.38	−1.08	2.15	−8.5	11.3
Defocus + Piston		$\sqrt{3}\ (2\rho^2 - 1)$	Z[4]	0.30	0.08	0.00	0.12		
Astigmatism-XY		$\sqrt{6}\rho^2\cos(2\theta)$	Z[5]	−0.27	0.40	0.32	−0.05		
Astigmatism-45		$\sqrt{6}\rho^2\sin(2\theta)$	Z[6]	−0.27	−0.37	−0.16	−0.18		
Coma-X + X-tilt		$2\sqrt{2}(3\rho^3 - 2\rho)\sin\theta$	Z[7]	−0.16	0.25	0.08	0.20		
Coma-Y + Y-tilt		$2\sqrt{2}(3\rho^3 - 2\rho)\cos\theta$	Z[8]	0.08	−0.03	−0.01	−0.03		
Trefoil		$2\sqrt{2}\rho^3\sin(3\theta)$	Z[9]	0.07	0.04	−0.03	0.04		
Trefoil		$2\sqrt{2}\rho^3\cos(3\theta)$	Z[10]	−0.13	0.07	0.01	−0.06		
Wavefront error (in peak-to-valley) [μm]				0.77	1.23	1.78	4.99		
Image quality (Hartmann constant) [arcsecs]				3.38		13.00			

Accuracy requirements (same as Table 1)	
Wavefront error (in peak-to-valley) [μm]	<38.8
Image quality (Hartmann constant) [arcsecs]	<33

2.3.4 Summary

We conducted the optical adjustment test of FITE using newly developed optical adjustment system. As a result, the installation errors of the two off-axis parabolic mirrors satisfied the accuracy required to detect the interference fringes at 155 μm (See Sec. 2.3.1). Optical adjustment results of FITE interferometer are listed below.

- Results of interferometer adjustment in the laboratory before shipping
  - ✧ Peak-to-valley wavefront errors of each off-axis parabolic mirror were 0.77 μm on the port-side and 1.23 μm on the starboard- side.
  - ✧ The Hartmann constant was 3.38 arcsecs.
- Results of interferometer adjustment before launch
  - ✧ Peak-to-valley wavefront error of each off-axis parabolic mirror was 1.78 μm on the port-side and 4.99 μm on the starboard-side.
  - ✧ The Hartmann constant was 13 arcsecs.

In addition, at the time of the adjustment in the laboratory, the required accuracy was satisfied to detect the interference fringe at the mid-infrared wavelength of 25 μm: the peak-to-valley wavefront error of each off-axis parabolic mirror was 12.5 μm, and the Hartmann constant was 5.5 arcsecs. Hence, this method has proven useful and has been successfully developed.

The interferometer adjustment test was finished before launch in Australia with the required accuracies, but significant residuals remained. Comparing these residuals with the analysis results using the optical design software Zemax OpticStudio®, all residuals of the first-order aberration term had an installation error of a specific degree of freedom of the off-axis parabolic mirror. Hence, each residual could be eliminated by the correction of the specific degree of freedom. Therefore, they could be adjusted to achieve the same accuracies as the results of interferometer adjustment in the laboratory.

3 Conclusion

In order to investigate the planet formation process, it is essentially effective to directly resolve the structures of protoplanetary disks in various wavelengths as well as to understand the properties of various types of the protoplanetary disks. Because the protoplanetary disks are recognized as the initial conditions of planetary system formation. For this purpose, it is necessary to perform observation with a high spatial resolution of less than one arcsecond. Large diameter of space telescopes with segmented mirros, which can provide a high spatial resolution, have been proposed for this porpose. James Webb Space Telescope: JWST (Acton et al., 2012), planned to be launch in 2021, consists segmented mirrors. In the second next generation, there are many plans that uses segmented larger mirrors space telescopes such as LUVOIR (Bolcar et al., 2016) and the Origins Space Telescope (The OST mission concept study team, 2018). However, increasing of the diameter of a space telescope by using segmented mirrors will eventually reach a limit. The future of high spatial resolution astronomy and astrophysics leaves no choice but to adopt the interferometer method.

In order to achieve high spatial resolution at the far-infrared wavelength region, we have developed the balloon-borne far-infrared interferometer, FITE. FITE has achieved the technology to observe in the far-infrared of 155 um with one-arcsecond order resolution. By conducting observations with high spatial resolution at the far-infrared wavelength (corresponding to the thermal radiation peak of cold to slightly warm dust), it is expected that the progress of planet formation theory and the formation of terrestrial planets will elucidate.

Since FITE is a two-beam interferometer, precise adjustment of the FITE interferometer optics is required before launch. We developed an interferometer adjustment system for FITE interferometer, and conducted the optical adjustment test of FITE by using it. As a result, the installation errors of the two off-axis parabolic mirrors were lower than the accuracy required to detect the interference fringes at 155 μm. Therefore, this new method has proven to be usable.

This newly developed adjustment instrument can simultaneously analyze the two beams of the FITE interferometer, thus making it possible to significantly reduce the adjustment period of the optical system. Usually the launching chance of a scientific balloon is severely limited not only by the speed of the surface wind but of the upper

wind. A few weeks of optics adjustment may often lead to miss a flight opportunity. In fact, long adjustment period was one of the major reason why FITE had not been launched in the previous campaigns. FITE tried balloon experiments in 2008 and 2010. At that time, the adjustment of the interferometer optics took two weeks to be ready-for-flight before the launch. On the other hand, in the Australia campaign of 2018, the adjustment was completed within three days only by using the newly developed system. The FITE payload successfully got into its flight ready state during the launching window.

This adjustment system developed for FITE interferometer enables remote adjustment for scientific balloon experiments. Therefore, it has the following possibilities; If the space telescope combined the remote measurement of wavefront error by the Shack-Hartmann wavefront sensor and the remote adjustment of the installation error, the interferometer adjustment could be carried out any time in space using a star as the light source. Therefore, this method is generally useful in space telescopes. There has never been an example of using a Shack-Hartmann wavefront sensor for a mirror adjustment of an installation error, at least in space telescopes. This is because, using the Shack-Hartmann wavefront sensor, it is necessary to install collimating optics at the focus of the mirror. In fact, JWST does not use the Shack-Hartmann wavefront sensor (Acton et al., 2012). Because the primary mirror of JWST consists of segmented mirrors, it is necessary to correct inherent uncertainty in the deployment of the optics and to find which segment corresponds to each beam from the acquired image (Acton et al., 2012). In a space telescope with segmented mirrors, it is possible to set collimating optics and measure the installation error with a Shack-Hartmann wavefront sensor. By re-imaging the pupil with collimating optics, the beam position does not move significantly on the Shack-Hartmann wavefront sensor. Therefore, it is not necessary to find which segmented mirror corresponds to which beam. Using the interferometer adjustment method for FITE, it is possible to measure the aberrations of a plurality of segmented mirrors from one image. Not only can the aberration of each segmented mirrors be measured, but also the aberration regarding a single mirror. Hence, the interferometer adjustment method for the FITE is more efficient than the JWST method.

The realization of a space interferometer is a major goal in the world including Europe and the United States. For instance, the underlying arguments for interferometers were recognized in the 2013 NASA Astrophysics Roadmap (Kouveliotou et al, 2014), and

NASA's exoplanet technology white paper roadmap[1] announced a plan to launch an optical infrared interferometer in space after 2035. To achieve space interferometry, it is necessary to promote technological development in steps. One of the goals of the FITE project is to become a precursor of the future space interferometers. In the case of a space interferometer, it is possible to increase the spatial resolution by changing the baseline length between the collecting plane mirrors. Since there is no space interferometer so far, the development of this new adjustment system may inspire the technology development for future space interferometers.

[1] https://exoplanets.nasa.gov/internal_resources/816.

Acknowledgement

I would like to express my deepest appreciation to Professor Hiroshi Shibai at Osaka University for his invaluable supports. I learned the importance of facing the experiment seriously, and of continuing to work hard even if it failed. He taught me the fun of experiments and the correct attitude as a researcher. This thesis could not be accomplished without his various advices. Prof. Shibai has been a researcher on the front line of infrared astronomy for a long time. Nevertheless, he provided me with research guidance even when he was busy. By the time Prof. Shibai retires from Osaka University, I am happy to complete my doctoral thesis to get a Ph.D. as the last graduated student. Since the FITE project is still on-going, I would appreciate his continued support.

I would like to greatly thank Professor Tetsuya Yoshida at the Scientific Ballooning Research and Operation Group, Institute of Space and Astronautical Science (ISAS), Japan Aerospace Exploration Agency (JAXA). He also taught me how to proceed with the balloon experiment necessary for a successful FITE experiment.

I am also deeply grateful to Professor Takahiro Sumi at Osaka University and Associate Professor Taro Matsuo at Nagoya University. Thanks to their cooperation, FITE was able to restart for the flight.

Finally, I want to thank to all of the FITE members and the Scientific Ballooning Research and Operation Group members who were involved in the FITE project, and my family who supported me for a long time.

References

Acton, D. S., Knight, J. S., Contos, A., Grimaldi, S., Terry, J., Lightsey, P., Barto, A., League, B., et al. [2012], Wavefront Sensing and Controls for the James Webb Space Telescope, Proc. SPIE 8442, 84422H

ALMA Partnership, Brogan, C. L., Pérez, L. M., Hunter, T. R., Dent, W. R. F., Hales, A. S., Hills, R. E., Corder, S., et al. [2010], First Results from High Angular Resolution ALMA Observations Toward the HL Tau Region, ApJL, 808, L3, p.10

Becklin, E. E., [2005], Stratospheric Observatory for Infrared Astronomy (SOFIA), Advances in Space Research, 36, p.1087

Bolcar, M. R., Feinberg, L., France, K., Rauscher, B. J., Redding, D., and Schiminovich, D., [2016], Initial technology assessment for the Large-Aperture UV-Optical-Infrared (LUVOIR) mission concept study," Proc. SPIE 9904, 99040J

Farrah, D., Smith, K. E., Ardila, D., Bradford, C., Dipirro, M., Ferkinhoff, C., Glenn, J., Goldsmith, P., et al. [2019], Review: Far-Infrared Instrumentation and Technology Development for the next Decade, J. Astron. Telesc. Instrum. Syst. 5, No. 2

Fukagawa, M., Tamura, M., Itoh, Y., Kudo, T., Imaeda, Y., Oasa, Y., Hayashi, S. S., and Hayashi M., [2006], Near-infrared images of protoplanetary disk surrounding HD 142527, ApJ, 636, L153

Hayashi, C., Nakazawa, K., Nakagawa, Y., [1985], Proto-stars and Planets II, 1100

Helmich, F., and Ivison, R., [2009], FIRI – a Far-infrared interferometer, Experimental Astronomy, V23, I1, p.245

Hillenbrand L. A., Carpenter, J. M., Kim, J. S., Meyer, M. R., Backman, D. E., Moro-Martin, A., Hollenbach, D. J., Hines, D. C., et al., [2008], ApJ, 677, 630

Ida, S., Lin, D. N. C, [2005], Toward a Deterministic Model of Planetary Formation. III. Mass Distribution of Short-Period Planets around Stars of Various Masses, ApJ, 626, 1045I

Kohyama, T., Shibai, H., Kawada, M., Watabe, T., Matsuo, T., Mochizuki, S., Matsumoto, Y., Morishita, H., et al. [2008], Far-infrared Interferometric Telescope Experiment: II. Sensor Optics, Proc. SPIE, 7013, 70133O

Kouveliotou, C., Agol, E., Batalha, N., Bean, J., Bentz, M., Cornish, N., Dressler, A., Figueroa-Feliciano, E., et al. [2014], Enduring Quests – Daring Visions (NASA Astrophysics in the Next Three Decades), NASA, http://go.nasa.gov/1gGVkZY

Lakshminarayanan, V., and Fleck, A., [2011], Zernike polynomials: a guide, Journal of Modern Optics, 58, No.7, p.545

Leisawitz, D., Baker, C., Barge, A., et al., [2007], The space infrared interferometric telescope (SPIRIT): High-resolution imaging and spectroscopy in the far-infrared, Advances in Space Research 40, 689-703

Mayor, M., and Queloz, D., [1995], A Jupiter-mass companion to a solar-type star, Nature, 378, 355

Michelson, A. A., and Pease, F. G., [1921], Measurement of the Diameter of alpha Orionis with the Interferometer, Astrophysical Journal, 53, p.249

Miyake. K., and Nakagawa, Y., [1993], Effects of Particle Size Distribution on Opacity Curves of Protoplanetary Disks around T Tauri Stars, ICARUS 106, 20

Muto, T., Grady, C. A., Hashimoto, J., Fukagawa, M., Hornbeck, J. B., Sitko, M., Russell, R., Werren, C., [2012], Discovery of small-scale spiral structures in the disk of SAO 206462 (HD 135344B): implications for the physical state of the disk from spiral density wave theory, APJL

Pilbratt, G. L., Riedinger, J. R., Passvogel, T., Crone, G., Doyle, D., Gageur, U., Heras, A. M., Jewell, C., et al. [2010], Herschel Space Observatory - An ESA facility for far-infrared and submillimetre astronomy, Astronomy and Astrophysics 518, L1

Rinehart, S. A., Dhabal, A., Fixsen, D., Juanola-Parramon, R., Leisawitz, D., Maher, S., Mentzell, J. E., Mundy, L., et al. [2018], The Balloon Experimental Twin Telescope for Infrared Interferometry (BETTII): first flight, Proc. SPIE, 10700, 107000F

Roelfsema, P. R., Shibai, H., Armus, L., Arrazola, D., Audard, M., Audley, M. D., Bradford, C. M., Charles, I., et al. [2018], SPICA – a large cryogenic infrared space telescope Unveiling the obscured Universe, PASA, 35

Sasaki, A., Shibai, H., Sumi, T., Fukagawa, M., Kanoh, T., Yamamoto, K., Itoh, Y., Aimi, Y., et al. [2012], Development of new optical adjustment system for FITE (Far-infrared Interferometric Telescope Experiment), Proc. SPIE 8445, 84452Z

Sasaki, A., Shibai, H., Sumi, T., Fukagawa, M., Kanoh, T., Yamamoto, K., Itoh, Y., Akiyama, N., et al. [2014], Far-infrared Interferometric Telescope Experiment: Optical Adjustment System, IEEE Transactions on Terahertz Science and Technology, 4, I2, p.179.

Sasaki, A., Shibai, H., Matsuo, T., Sumi, T., Itoh, S., Ohyama, T., Tani, Y., Saiki, M., et al. [2019], Optical adjustment of the FITE interferometer, JAI, in press

Shibai, H., Fukagawa, M., [2009], Toward comprehensive models of protoplanetary disks, 天文月報, 102, 190

Shibai, H., Fukagawa, M., Kato, E., Kanoh, T., Kohyama, T., Itoh, Y., Yamamoto, K., Kawada, M., et al. [2010], Far-infrared Interferometric Telescope Experiment (FITE): Toward the First Flight, Pathways Towards Habitable Planets, p.541

The OST mission concept study team, [2018], The Origins Space Telescope (OST) Mission Concept Study Interim Report, preprint, (arXiv:1809.09702)

Watanabe, M., Takami, H., Takato, N., Colley, S., Eldred, M., Kane, T., Guyon, O., Hattori, M., et al. [2004], Design of the Subaru laser guide star adaptive optics module, Proc. SPIE, 5490, p.1096

Wild, W., de Graauw, T., Helmich, F., et al., [2008], ESPRIT: a study concept for a far-infrared interferometer in space, in Optical and Infrared Interferometry, Proc. SPIE 7013, 70132R

Wizinowich, P., Le Mignant, D., Bouchez, A. H., Campbell, R. D., Chin, J. C. Y., Contos, A. R., van Dam, M. A., Hartman, S. K., et al. [2006], The W. M. Keck Observatory Laser Guide Star Adaptive Optics System: Overview, The Astronomical Society of the Pacific, 118, p.297

Wyatt, M. C., [2008], Evolution of Debris Disks, Annu. Rev. Astron. Astrophys, 44, 339-83

Appendix A

Alignment mechanism of the off-axis parabolic mirrors for FITE: λ-pod

Fig. A.1a shows the newly developed an alignment mechanism of the off-axis parabolic mirrors for FITE, called lambda-pod (λ-pod). Its structure is like a combination of three "λ" words: This is the reason why we called it "λ-pod". It is based on a quasi-parallel mechanism that can control the mirror position; the translation in the X/Y/Z directions and the rotation around X/Y/Z axes of the mirror are performed by changing the lengths of six direct motion actuators. Although its structure resembles a Stewart platform, there are differences in the connection method of the direct motion actuators. In the case of the Stewart platform, we must control the six direct motion actuators all together. In the case of λ-pod, each direct motion actuator can be controlled individually. It able to be controlled by moving only one direct motion actuator. We reduced the risk of malfunction for the quasi-parallel mechanism.

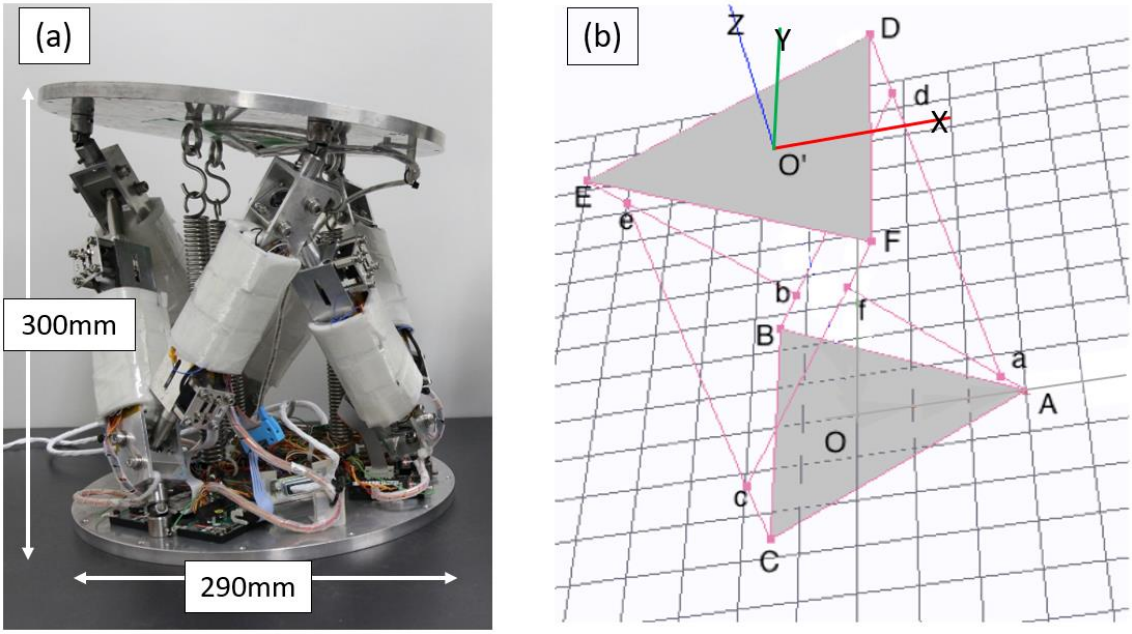

Fig. A.1 (a) Appearance of the λ-pod. The off-axis parabolic mirror is mounted on the upper plate in this figure. (b) Coordinate system of the λ-pod.

When adjusting the parabolic mirror using the λ-pod, we change the configuration of these motion actuators. Since, each actuator is considered to be a rigid body, its configuration can be represented by six parameters, i.e., position and orientation in the three-dimensional coordinates. The lengths of the actuators are obtained by a calculation described below. Fig. A.1b shows the coordinate of the λ-pod. While a plane created by the triangle ABC represents the base (reference) plate of the lambda-pod, that created by the triangle DEF does the end (output) plate. X/Y/Z axes in this coordinate system are fixed on the end plate. The origin is indicated by O'. After we move the actuators, the coordinate system on the end plate is changed. The position and orientation of this new (xyz) coordinate system with respect to the original (XYZ) one is specified by a parameter set of (x, y, z, α, β, γ). Here (x, y, z) is the position vector of the origin O 'of the (xyz) coordinate system, and (α, β, γ) is the Euler angles, which are measured around the z-x-z axes in this order. of the z-x-z system in this order. The calculation to determine the lengths of the six legs (motor) from the six coordinates of the points d, e, f, D, E, and F required to solve an 18-dimensional nonlinear system of equations. In order to find a solution quickly during observation, we applied a first-order polynomial approximation to the equations to reduce the calculation. As a result of the adjustment test, the adjustment by the λ-pod was found to be controllable; the accuracy of the adjustment was within 2 μm in the direction of the optical axis and within 2 arcseconds in the direction of the mirror tilt.

Appendix B

List of Publications

Refereed Papers

International

1. “Optical adjustment of the FITE interferometer”
   Sasaki, A., Shibai, H., Matsuo, T., Sumi, T., Itoh, S., Ohyama, T., Tani, Y., Saiki, M., Tsuboi, T., Narita, M.
   Journal of Astrophysical Instrument, in press, 2019

2. “Far-infrared Interferometric Telescope Experiment: Optical Adjustment System”
   Sasaki, A., Shibai, H., Fukagawa, M., Sumi, T., Kanoh, T., Yamamoto, K., Itoh, Y., Akiyama, N., Terano, A., Aimi, Y., Kuwada, Y., Konishi, M., Narita, M.
   IEEE Transactions on Terahertz Science and Technology, vol. 4, I2, p.179, 2014
   doi: 10.1109/TTHZ.2013.2296996

Conference Proceedings

International

3. “Development of new optical adjustment system for FITE (Far-infrared Interferometric Telescope Experiment)”
   Sasaki, A., Shibai, H., Sumi, T., Fukagawa, M., Kanoh, T., Yamamoto, K., Itoh, Y., Aimi, Y., Kuwada, Y., Kaneko, Y., Konishi, M., Sai, S., Akiyama, N., Narita, M.
   Optical and Infrared Interferometry III. Proceedings of the SPIE, Vol. 8445, article id. 84452Z, 2012

Appendix C

List of Presentations

Oral Presentations

Domestic

1. 宇宙遠赤外線干渉計（FITE）プロジェクト：次期フライト計画
佐々木彩奈, 松尾太郎, 芝井 広, 伊藤哲史, 金田英宏
大気球シンポジウム 2019 年度, isas19-sbs-026, ISAS, 2019 年 11 月

2. “気球搭載遠赤外線干渉計 FITE 実験結果”
芝井 広, 佐々木彩奈, 伊藤哲司, 大山照平, 大塚愛里梨, 谷 貴人, 佐伯守人, 坪井隆浩, 住 貴宏, 松尾太郎, 成田正直, 土居明広, 吉田哲也, 斎藤芳隆, 河野裕介, Stephen Reinhart
大気球シンポジウム平成 30 年度, isas18-sbs-017, 2018 年 11 月

3. “遠赤外線干渉計 FITE：豪州での光学系調整結果”
佐々木彩奈, 芝井 広, 住 貴宏, 松尾太郎, 須藤 淳, 伊藤哲司, 大山照平, 佐伯守人, 坪井隆浩, 成田正直
大気球シンポジウム平成 30 年度, isas18-sbs-018, 2018 年 11 月

4. “気球搭載遠赤外線干渉計 FITE 実験経過”
芝井 広, 住 貴宏, 松尾太郎, 須藤 淳, 伊藤哲司, 大山照平, 大塚愛里梨, 谷 貴人, 佐伯守人, 坪井隆浩, 吉田哲也, 齊藤芳隆, 成田正直, 佐々木彩奈, 土居明広, 河野裕介
日本天文学会 2018 年秋季年会, V214a, 兵庫県立大学, 2018 年 9 月

5. “気球搭載型遠赤外線干渉計 FITE のフライトに向けた干渉計調整結果”
佐々木彩奈, 芝井 広, 住 貴宏, 松尾太郎, 伊藤哲司, 大山照平, 谷 貴人, 佐伯守人, 坪井隆浩, 成田正直
日本天文学会 2018 年秋季年会, V215a, 兵庫県立大学, 2018 年 9 月

6. “気球搭載遠赤外線干渉計 FITE の準備状況報告”
芝井 広, 佐々木彩奈, 伊藤哲司, 大山照平, 大塚愛里梨, 谷 貴人, 佐伯守人, 坪井 隆浩, 住 貴宏, 松尾太郎, 成田正直, 土居明広, 吉田哲也, 斎藤芳隆, 河野裕介, Stephen Reinhart
大気球シンポジウム平成 29 年度, isas17-sbs-022, 2017 年 11 月

7. “遠赤外線干渉計 FITE の光学系状況報告”
佐々木彩奈, 芝井 広, 住 貴宏, 松尾太郎, 須藤 淳, 伊藤哲司, 大山照平, 佐伯守人, 坪井隆浩, 成田正直
大気球シンポジウム平成 29 年度, isas18-sbs-023, 2017 年 11 月

8. “気球搭載遠赤外線干渉計 FITE の準備状況報告”
芝井 広, 佐々木彩奈, 伊藤哲司, 大山照平, 大塚愛里梨, 谷 貴人, 住 貴宏, 松尾太郎, 須藤 淳, 辰巳耕介, 成田正直, 土居明広, 吉田哲也, 斎藤芳隆, 河野裕介, Stephen Reinhart
大気球シンポジウム平成 28 年度, isas16-sbs-022, 2016 年 11 月

9. “気球搭載遠赤外線干渉計 FITE”
芝井 広、佐々木彩奈、伊藤哲司, 中道みのり, 大山照平, 谷 貴人, 住 貴宏, 松尾太郎, 小西美穂子, 山本広大, 成田正直, 土居明広, 吉田哲也、斉藤芳隆, 河野裕介
大気球シンポジウム平成 27 年度, isas15-sbs-041, 2015 年 11 月

10. “気球搭載遠赤外線干渉計 FITE”
芝井 広、佐々木彩奈、寺農 篤, 伊藤哲司, 中道みのり, 大山照平, 密本万吉, 住 貴宏, 深川美里, 桑田嘉大, 小西美穂子, 山本広大, 成田正直, 土居明広, 吉田哲也、斉藤芳隆, 河野裕介
大気球シンポジウム平成 26 年度, isas14-sbs-025, 2014 年 11 月

11. “気球搭載遠赤外線干渉計 FITE : 放物面鏡調整機構の開発”
寺農 篤, 芝井 広, 佐々木彩奈, 伊藤哲司, 中道みのり, 住 貴宏, 深川美里, 桑田嘉大, 小西美穂子, 山本広大, 成田正直
大気球シンポジウム平成 26 年度, isas14-sbs-026, 2014 年 11 月

12. “FITE 用圧縮型 Ge:Ga 二次元遠赤外線アレイの開発-II”
芝井 広, 秋山直輝, 中道みのり, 山本広大, 佐々木彩奈, 寺農 篤, 伊藤哲司, 内賀嶋 瞭, 住 貴宏, 深川美里, 會見有香子, 桑田嘉大, 小西美穂子
日本天文学会 2014 年春季年会, W211a, 国際基督教大学, 2014 年 3 月

13. “気球搭載型遠赤外線干渉計 FITE: 次期フライト計画と高強度フレームの開発”
芝井 広, 山本広大, 佐々木彩奈, 秋山直輝, 寺農 篤, 住 貴宏, 深川美里, 會見有香子, 桑田嘉大, 小西美穂子, 成田正直, 吉田哲也, 斉藤芳隆, 土居明広, 河野裕介
大気球シンポジウム平成 25 年度, isas13-sbs-024, 2013 年 11 月

14. “気球搭載型遠赤外線干渉計 FITE：次期フライト計画と高強度フレームの開発”
芝井 広, 山本広大, 佐々木彩奈, 秋山直輝, 寺農 篤, 住 貴宏, 深川美里, 會見有香子, 桑田嘉大, 小西美穂子, 成田正直, 吉田哲也, 斉藤芳隆, 土居明広, 河野裕介
日本天文学会 2013 年秋季年会, W206a, 東北大学, 2013 年 9 月

15. “遠赤外線干渉計 FITE: 新干渉計調整機構の開発”
佐々木彩奈, 芝井 広, 山本広大, 秋山直輝, 寺農 篤, 伊藤哲司, 住 貴宏, 深川美里, 會見有香子, 桑田嘉大, 小西美穂子, 成田正直
日本天文学会 2013 年秋季年会, W207a, 東北大学, 2013 年 9 月

16. “宇宙遠赤外線干渉計（FITE）プロジェクト：次回フライトに向けて”
芝井 広, 住 貴宏, 深川美里, 叶 哲生, 伊藤優佑, 山本広大, 會見有香子, 桑田嘉大, 小西美穂子, 佐々木彩奈, 秋山直輝, 成田正直, 吉田哲也, 斉藤芳隆
大気球シンポジウム平成 24 年度, isas12-sbs-032, 2012 年 10 月

Poster Presentations

International

17. “Far-infrared Interferometric Telescope Experiment: FITE”
Sasaki,A., Shibai, H., Fukagawa, M., Sumi, T., Yamamoto, K., Itoh, Y., N., Terano, A., Kuwada, Y., Konishi, M., Narita, M.
Pathways towards habitable planets Ⅱ
July13-17, 2015 Bern, Switzerland

18. “Balloon Borne Astronomical Interferometer in Far-infrared”
Sasaki, A., Shibai, H., Kanoh, T., Yamamoto, K., Akiyama, N., Sumi, T., Fukagawa, M., Aimi, Y., Kuwada, Y., Konishi, M., Narita, M.
Origins 2014, ISSOL-the International Astrobiology Society and Bioastronom
July 6-11, 2014, Nara, Japan,

19. “Development of New Optical Adjustment System for FITE”
Sasaki, A., Shibai, H., Kanoh, T., Yamamoto, K., Akiyama, N., Sumi, T., Fukagawa, M., Aimi, Y., Kuwada, Y., Konishi, M., Narita, M.
International Symposium on Research Frontiers of Physics, Earth and Space Science
Dec.17 and 18, 2013, Toyonaka campus of Osaka University, Japan

20. “ Development of New Optical Adjustment system for FITE (Far-Infrared Interferometric Experiment)”
Sasaki, A., Shibai, H., Kanoh, T., Yamamoto, K., Akiyama, N., Sumi, T., Fukagawa, M., Aimi, Y., Kuwada, Y., Konishi, M., Narita, M.
International Symposium on Space Terahertz Technology
April 8-10, 2013 Groningen, The Netherland

21. “Development of New Optical Adjustment System for FITE (Far-Infrared Interferometric Telescope Experiment)”
Sasaki, A., Shibai, H., Sumi, T., Fukagawa, M., Kanoh, T., Yamamoto, K., Itoh, Y., Aimi, Y., Kuwada, Y., Kaneko, Y., Konishi, M., Syoko, S., Akiyama, N., Narita, M.
SPIE Astronomical Telescopes + Instrumentation, July 1-6, 2012, Amsterdam

Domestic

22. “地球型系外惑星の分光観測を目指した宇宙赤外線干渉計”
松尾太郎, 五十里哲, 石渡 翔, 近藤宙貴, 河野 功, 伊藤琢博, 藤井友香, 川村静児, 佐々木彩奈, 伊藤哲司, 芝井 広, 住 貴宏, 金田英宏, Stephen A. Rinehart, Elmer Sharp, Martin Turbet
宇宙科学シンポジウム, P2-12, ISAS, 2019 年 12 月

23. “遠赤外線干渉計 FITE フライト計画”
芝井 広, 住 貴宏, 松尾太郎, 須藤 淳, 伊藤哲司, 大塚愛里梨, 谷 貴人, 佐伯守人, 坪井隆浩, 吉田哲也, 齊藤芳隆, 成田正直, 佐々木彩奈, 土居明広, 河野裕介
日本天文学会 2017 年秋季年会, V209b, 北海道大学, 2017 年 9 月

24. “気球搭載型遠赤外線干渉計(FITE)干渉光学系の進捗報告”
佐々木彩奈, 芝井 広, 伊藤哲司, 大山照平, 大塚愛里梨, 谷 貴人, 須藤 淳,

住 貴宏, 松尾太郎, 成田正直
宇宙科学シンポジウム, P-154, ISAS, 2017 年 1 月

25. “FITE 用信号読み出し回路の改良と遠赤外線センサーの感度測定”
大山照平, 芝井 広, 佐々木彩奈, 秋山直樹, 中道みのり, 伊藤哲司, 谷 貴人, 大塚愛里梨, 住 貴宏, 深川 美里, 松尾太郎, 成田正直
日本天文学会 2016 年秋季年会, V205b, 愛媛大学, 2016 年 9 月

26. “FITE：スターカメラ用星像中心検出プログラムの高速化”
伊藤哲司, 芝井 広, 佐々木彩奈, 中道みのり, 大山照平, 谷 貴人, 桑田嘉大, 小西美穂子, 須藤 淳, 住 貴宏, 山本広大, 成田正直
日本天文学会 2015 年秋季年会, V229b, 甲南大学, 2015 年 9 月“気球搭載型遠赤外線干渉計 FITE: 結像光学系の要求性能評価と公差解析”
伊藤哲司, 芝井 広, 佐々木彩奈, 寺農 篤, 中道みのり, 住 貴宏, 深川美里, 桑田嘉大, 小西美穂子, 須藤 淳, 山本広大, 成田正直
日本天文学会 2015 年秋季年会, W207b, 山形大学, 2015 年 9 月

27. “遠赤外線干渉計 FITE：放物面鏡調整機構の開発”
寺農 篤, 芝井 広, 佐々木彩奈, 伊藤哲司, 中道みのり, 住 貴宏, 深川美里, 桑田嘉大, 小西美穂子, 山本広大, 成田正直
日本天文学会 2014 年秋季年会, W208b, 山形大学, 2014 年 9 月

28. “遠赤外線干渉計 FITE の新干渉計調整機構とその光学系の開発”
佐々木彩奈, 芝井 広, 叶 哲生, 伊藤優佑, 山本広大, 秋山直輝, 住 貴宏, 深川美里, 會見有香子, 桑田嘉大, 小西美穂子, 成田正直
日本天文学会 2013 年春季年会, W15c, 埼玉大学, 2013 年 3 月

29. “遠赤外線干渉計 FITE: 新長軽量平面鏡の開発”
叶 哲生, 芝井 広, 伊藤優佑, 山本広大, 佐々木彩奈, 秋山直輝, 住 貴宏, 深川美里, 會見有香子, 桑田嘉大, 小西美穂子, 成田正直
日本天文学会 2013 年春季年会, W16c, 埼玉大学, 2013 年 3 月

30. “FITE 用新放物面鏡調整機構の開発”
片多修平, 秋山直輝, 芝井 広, 叶 哲生, 伊藤優佑, 山本広大, 佐々木彩奈, 住 貴宏, 深川美里, 會見有香子, 桑田嘉大, 小西美穂子, 成田正直
日本天文学会 2013 年春季年会, W17c, 埼玉大学, 2013 年 3 月

31. “FITE 用遠赤外線圧縮型 Ge:Ga 二次元アレイセンサの開発”
秋山直輝, 芝井 広, 伊藤優佑, 叶 哲生, 山本広大, 佐々木彩奈, 住 貴宏, 深川美里, 會見有香子, 桑田嘉大, 小西美穂子, 成田正直
日本天文学会 2013 年春季年会, W18c, 埼玉大学, 2013 年 3 月

32. “気球搭載型遠赤外線干渉計 FITE：2010 年実験結果と次期フライト計画”
芝井 広、住 貴宏、深川美里、叶 哲生、幸山常仁、伊藤優佑、山本広大、会見有香子、金子有紀、桑田嘉大、Dimitrios Kontopoulos、小西美穂子、蔡 承亨、佐々木彩奈、秋山直輝、白井皓寅、加藤恵理、成田正直、吉田哲也、斉藤芳隆、下浦美那、Antonio Mario Magalhaes、Jose William Villas-Boas
日本天文学会 2012 年春季年会, W211c, 龍谷大学, 2012 年 3 月

33. “WFS を用いた遠赤外線干渉計 FITE の光学調整方法の開発”
佐々木彩奈、芝井 広、住 貴宏、深川美里、叶 哲生、伊藤優佑、山本広大、会見有香子、金子有紀、桑田嘉大、Dimitrios Kontopoulos、蔡 承亨、秋山直輝、白井皓寅、成田正直
日本天文学会 2012 年春季年会, W212b, 龍谷大学, 2012 年 3 月